

EFFECTS OF GEOMETRIC FEATURES AND SIZE ON THE SCATTERING  
BEHAVIOR OF NANOPARTICLES FOR INDEPENDENT SCATTERING  
REGIME

by

Yasin Alperen Yalçı

B.S., Mechanical Engineering, Boğaziçi University, 2019

Submitted to the Institute for Graduate Studies in  
Science and Engineering in partial fulfillment of  
the requirements for the degree of  
Master of Science

Graduate Program in Mechanical Engineering  
Boğaziçi University

2023

## ACKNOWLEDGEMENTS

First of all, I would like to express my gratitude to my advisor Prof. Hakan Ertürk for his guidance, enthusiasm and patience throughout my research. He always encourages me to do very best in my thesis study. I would also like to thank Prof. Tuba Okutucu Özyurt and Assoc. Prof. Nazlı Dönmezer for accepting to be in my thesis committee despite their tight schedules. I would like to also thank all of my TESLab colleagues.

I am grateful to TÜBİTAK for their financial support throughout this study under the 2210/A program.

I would like to thank my mother Nesrin, my father Celil and my brother Oğuzhan for everything I have achieved. It would be impossible without your love and support. Last but not least, I would like to express my deepest gratitude to my beautiful partner Hazal Ekin for her support, understanding and unconditional love.

## ABSTRACT

### **EFFECTS OF GEOMETRIC FEATURES AND SIZE ON THE SCATTERING BEHAVIOR OF NANOPARTICLES FOR INDEPENDENT SCATTERING REGIME**

With the fast development of nanotechnology in recent years, the detection and characterization of nanoparticles have grown in importance. Due to their effectiveness and robustness, optical techniques are widely employed for nanoparticle detection and characterization. Although there are several studies on absorption parameters, there are comparatively few studies on the influence of size and shape on scattering parameters. This research intends to address this void by examining scattering parameters for gold nanoparticles of varying size and shape. For this inquiry, COMSOL is used to develop a finite element model that permits working with various forms and sizes. The results indicate that the impacts of edges and a higher aspect ratio result in a higher scattering efficiency and peak resonance wavelength. It has also been shown that the redshift of the resonance wavelength is mainly due to the increase of aspect ratio. The investigation of scattering dispersion reveals that the scattering over polar angle is symmetric at resonance wavelengths but asymmetric at other wavelengths. However, shape factors such as edges and aspect ratio change exacerbate the asymmetries of scattering at polar angles. The effects of the presence of corners can be distinguished only by examining the dispersion of the scattered light. The statistical analysis is carried out for the determination of impact ratios of shape parameters on the scattering efficiency, the resonance wavelength and the asymmetry of the scattering. These investigations demonstrate that the shape and size of gold nanoparticles may be determined by analysing scattering properties, and this work offers the data necessary for this estimation within specific constraints.

## ÖZET

# BAĞIMSIZ SAÇILMA REJİMİ İÇİN GEOMETRİK ÖZELLİKLERİN VE BOYUTUN NANOPARÇACIKLARIN SAÇILMA DAVRANIŞI ÜZERİNDEKİ ETKİSİ

Son yıllarda nanoteknolojinin hızlı gelişimi ile nanopartiküllerin tespiti ve karakterizasyonu önem kazanmıştır. Etkinlikleri ve sağlamlıkları nedeniyle, optik teknikler nanoparçacık tespiti ve karakterizasyonu için yaygın olarak kullanılmaktadır. Absorpsiyon parametreleri üzerine çeşitli çalışmalar olmasına rağmen, boyut ve şeklin saçılma parametreleri üzerindeki etkisine ilişkin nispeten az sayıda çalışma vardır. Bu araştırma, değişen boyut ve şekle sahip altın nanopartiküller için saçılma faktörlerini inceleyerek bu boşluğu doldurmayı amaçlamaktadır. Bu araştırma için COMSOL, çeşitli şekil ve boyutlarda çalışmaya izin veren bir sonlu eleman modeli geliştirmek için kullanıldı. Sonuçlar, kenarların etkilerinin ve daha yüksek bir en-boy oranının, daha yüksek bir saçılma verimliliği ve tepe rezonans dalga boyu ile sonuçlandığını göstermektedir. Rezonans dalga boyunun kırmızıya kaymasının esas olarak en-boy oranının artmasından kaynaklandığı da gösterilmiştir. Saçılma dağılımının araştırılması, kutup açısı üzerindeki saçılmanın rezonans dalga boylarında simetrik, ancak diğer dalga boylarında asimetric olduğunu ortaya koymaktadır. Bununla birlikte, kenarlar ve en-boy oranı gibi şekil faktörleri, kutup açılarında saçılmanın asimetriclerini şiddetlendirir. Köşelerin varlığının etkileri, yalnızca saçılan ışığın dağılımı incelenerek ayırt edilebilir. Şekil parametrelerinin saçılma verimi, rezonans dalga boyu ve saçılmanın asimetricisi üzerindeki etki oranlarının belirlenmesi için istatistiksel analiz yapıldı. Bu araştırmalar, altın nanopartiküllerin şeklinin ve boyutunun, saçılma özelliklerinin analiz edilmesiyle belirlenebileceğini göstermektedir ve bu çalışma, bu tahmin için gerekli verileri belirli kısıtlamalar dahilinde sunmaktadır.

## TABLE OF CONTENTS

ACKNOWLEDGEMENTS . . . . .	iii
ABSTRACT . . . . .	iv
ÖZET . . . . .	v
LIST OF FIGURES . . . . .	viii
LIST OF TABLES . . . . .	xiii
LIST OF SYMBOLS . . . . .	xiv
LIST OF ACRONYMS/ABBREVIATIONS . . . . .	xvi
1. INTRODUCTION . . . . .	1
1.1. Optical Characterization of Nanoparticles . . . . .	1
1.2. Literature Review . . . . .	4
1.3. Objective of the Study . . . . .	7
2. FORMULATION AND METHOD . . . . .	9
2.1. Formulation of Light Scattering by a Particle . . . . .	9
2.1.1. Electromagnetic Wave in Free Space . . . . .	9
2.1.2. Scattering Cross Section . . . . .	10
2.2. Finite Element Method for Light Scattering . . . . .	11
2.3. Problem Statement . . . . .	17
3. VALIDATION AND REFINEMENT . . . . .	19
3.1. Validation and Mesh Refinement of Spherical Objects . . . . .	19
3.1.1. Validation and Mesh Refinement for Efficiency Calculations . . . . .	19
3.1.2. Validation and Mesh Refinement for $S_{11}$ Calculations . . . . .	23
3.2. Mesh Refinement and Orientation Averaging of Asymmetric Objects . . . . .	26
3.2.1. Mesh Refinement of Asymmetric Objects . . . . .	26
3.2.2. Orientation Averaging . . . . .	28
4. RESULTS AND DISCUSSIONS . . . . .	34
4.1. Scattering Efficiency Results . . . . .	34
4.2. Directional Distribution of Scattered Intensity . . . . .	54
5. CONCLUSIONS . . . . .	60

REFERENCES . . . . .	63
APPENDIX A: FINITE ELEMENT MODEL IN COMSOL . . . . .	70
APPENDIX B: ADDITIONAL PLOTS . . . . .	75

## LIST OF FIGURES

Figure 2.1.	Electric and magnetic fields that accompanying EM wave. . . . .	9
Figure 2.2.	Geometry of the model. . . . .	14
Figure 2.3.	Meshing of the geometry. . . . .	15
Figure 2.4.	The parameterized surface. . . . .	17
Figure 2.5.	Nanoparticles which are investigated throughout this study. . . . .	18
Figure 3.1.	Scattering efficiency of 50 nm AuNP. . . . .	20
Figure 3.2.	Computation time and MAE of 50 nm AuNP for different mesh sizes. . . . .	21
Figure 3.3.	Scattering efficiency of 200 nm AuNP. . . . .	22
Figure 3.4.	Computation time and MAE of 200 nm AuNP for different mesh sizes. . . . .	23
Figure 3.5.	$S_{11}$ through the polar angle for different mesh sizes of 50 nm AuNP. . . . .	24
Figure 3.6.	Computation time of $S_{11}$ and MAE of mesh elements of 50 nm AuNP for different mesh sizes. . . . .	25
Figure 3.7.	$S_{11}$ through the polar angle at finer mesh size for 100 nm AuNP. . . . .	25
Figure 3.8.	Scattering efficiencies of the ellipsoid with different mesh sizes. . . . .	26

Figure 3.9.	Scattering efficiencies of the cube with different mesh sizes and corner refinement. . . . .	27
Figure 3.10.	Meshing of cube a) with and b) without corner refinement. . . . .	27
Figure 3.11.	Square prism at arbitrary different orientations for orientation averaging at (a) long edge parallel to y axis (b) long edge parallel to x axis (c) long edge rotated 45° around z axis (d) long edge rotated 45° around all axes. . . . .	29
Figure 3.12.	Comparison of scattering cross sections calculated averaging and numerical integration. . . . .	30
Figure 3.13.	$S_{11}$ by the polar angle with different orientations for cube AuNP whose edge is 50 nm. . . . .	31
Figure 3.14.	$S_{11}$ through the polar angle with different orientations for ellipsoid AuNP. . . . .	32
Figure 4.1.	Scattering efficiencies over incident wavelength with different sized particles a) sphere b) ellipsoid 1.5 c) ellipsoid 2 d) ellipsoid 3 e) cylinder 1 f) cylinder 1.5. . . . .	37
Figure 4.2.	Scattering efficiencies over incident wavelength with different sized particles a) cylinder 2 b) cylinder 3 c) cube d) square prism 1.5 e) square prism 2 f) square prism 3. . . . .	38
Figure 4.3.	Scattering efficiencies over incident wavelength for particles with different aspect ratios a) spheroid 50 nm, b) spheroid 60 nm, c) spheroid 70 nm, d) spheroid 80 nm. . . . .	39

Figure 4.4.	Scattering efficiencies over incident wavelength for particles with different aspect ratios a) cylinder 50 nm, b) cylinder 60 nm, c) cylinder 70 nm, d) cylinder 80 nm, e) prism 50 nm, f) prism 60 nm.	40
Figure 4.5.	Scattering efficiencies over incident wavelength for particles with different aspect ratios a) prism 70 nm, b) prism 80 nm. . . . .	41
Figure 4.6.	Electric field distribution around 50 nm a) ellipsoid, AR=1.5 b) ellipsoid AR=3. . . . .	42
Figure 4.7.	Scattering efficiencies over incident wavelength for particles with different edges and corners a) AR1 50 nm b) AR1 60 nm c) AR1 70 nm d) AR1 80 nm. . . . .	43
Figure 4.8.	Scattering efficiencies over incident wavelength for particles with different edges and corners a) AR1.5 50 nm b) AR1.5 60 nm c) AR1.5 70 nm d) AR1.5 80 nm e) AR2 50 nm f) AR2 60 nm. . . .	44
Figure 4.9.	Scattering efficiencies over incident wavelength for particles with different edges and corners a) AR2 70 nm b) AR2 80 nm c) AR3 50 nm d) AR3 60 nm e) AR3 70 nm f) AR3 80 nm. . . . .	45
Figure 4.10.	Electric field distribution around 50 nm cylinder, AR=1.5. . . . .	46
Figure 4.11.	Electric field distribution around 50 nm cylinder, AR=3. . . . .	47
Figure 4.12.	Electric field distribution around 50 nm square prism, AR=1.5. . . .	47
Figure 4.13.	Electric field distribution around 50 nm square prism, AR=3. . . .	48

Figure 4.14. Scattering efficiencies over incident wavelength for the particles that have the same shape and cross-sectional area. . . . .	49
Figure 4.15. Scattering efficiencies over incident wavelength for the particles that have the same aspect ratio and cross-sectional area. . . . .	50
Figure 4.16. Scattering efficiencies over incident wavelength for the particles that have the a) same aspect ratio and b) cross-sectional area. . . . .	51
Figure 4.17. The importance parameters on a) peak scattering efficiency b) resonance wavelength. . . . .	53
Figure 4.18. $S_{11}$ values over polar angle for a) lowest $\lambda = 520$ nm and b) highest $\lambda = 720$ nm incident wavelength. . . . .	55
Figure 4.19. Normalized $S_{11}$ values over polar angle for a) lowest $\lambda = 520$ nm and b) highest $\lambda = 720$ nm incident wavelength. . . . .	56
Figure 4.20. Asymmetry factors at different wavelengths for particles a) AR1 b) AR1.5 c) AR2 d) AR3. . . . .	58
Figure 4.21. Asymmetry factors at different wavelengths for particles a) Spheroid b) Cylinder c) Prism. . . . .	59
Figure 4.22. Pareto chart for asymmetry factors. . . . .	59
Figure A.1. Model node tree in COMSOL. . . . .	70
Figure B.1. Variability chart for the peak scattering efficiency. . . . .	75
Figure B.2. Variability chart for the resonance wavelength. . . . .	75

Figure B.3.	a) Nominal b) Normalized $S_{11}$ values over polar angle for $\lambda = 540$ nm. . . . .	76
Figure B.4.	a) Nominal b) Normalized $S_{11}$ values over polar angle for $\lambda = 550$ nm. . . . .	76
Figure B.5.	a) Nominal b) Normalized $S_{11}$ values over polar angle for $\lambda = 570$ nm. . . . .	77
Figure B.6.	a) Nominal b) Normalized $S_{11}$ values over polar angle for $\lambda = 580$ nm. . . . .	77
Figure B.7.	a) Nominal b) Normalized $S_{11}$ values over polar angle for $\lambda = 610$ nm. . . . .	78
Figure B.8.	a) Nominal b) Normalized $S_{11}$ values over polar angle for $\lambda = 650$ nm. . . . .	78

## LIST OF TABLES

Table 2.1.	Background Electric Field [V/m]. . . . .	15
Table 2.2.	Variables definition for results. . . . .	16
Table 2.3.	Expressions for the parameterized surface. . . . .	16
Table 2.4.	Dimensions of nanoparticles in terms of diameter of the sphere (D). . . . .	18
Table 3.1.	Number of mesh elements for each mesh sizes for denoted NPs. . . . .	20
Table 3.2.	Total number angles needed for convergence of results. . . . .	33
Table 4.1.	Average geometric cross sections in [ $nm^2$ ] of NPs for different D values. . . . .	34
Table 4.2.	Peak scattering efficiency values at resonance wavelengths. . . . .	35
Table 4.3.	Resonance wavelengths of each particle. . . . .	36
Table 4.4.	$R^2$ and mean absolute percentage errors for each dataset. . . . .	52
Table 4.5.	Importance of each parameter on scattering efficiency. . . . .	52
Table A.1.	Parameters inputs in Global Definitions group. . . . .	71
Table A.2.	Entries in Variables Subgroup. . . . .	72
Table A.3.	Parametric Sweep for wavelength analysis. . . . .	73

## LIST OF SYMBOLS

$C_a$	Absorption cross section
$C_e$	Extinction cross section
$C_s$	Scattering cross section
$C_{s,avg}$	Scattering cross section averaged over orientation
$c_0$	Speed of light in free space
$D$	Diameter of sphere / Characteristic length
$\vec{E}$	Electric Field
$E_0$	Electromagnetic field
$f$	Optical property
$G$	Geometric cross section
$G_{avg}$	Geometric cross section averaged over orientation
$\vec{H}$	Magnetic Field
$i$	Imaginary number
$I_i$	Intensity of incident wave
$I_s$	Intensity of scattered wave
$k$	Wave number
$K$	Imaginary part of the complex refractive index
$n$	Real part of the complex refractive index
$\bar{n}$	Complex refractive index
$\vec{n}$	Normal vector
$N$	Total number of angles of measurement
$Q_h$	Total power dissipation density
$Q_a$	Absorption efficiency
$Q_{s,avg}$	Scattering efficiency averaged over orientation
$r$	Far field distance
$r_{pml}$	Radius of domain
$r_s$	Radius of sphere
$\vec{S}$	Poynting Vector

$S_{11}$	First element of the scattering matrix
$t_{pml}$	Thickness of PML
$Z_0$	Impedance of free space
$\lambda_{max}$	Final wavelength
$\lambda_{min}$	Initial wavelength
$\lambda_{step}$	Step wavelength
$\mu_0$	Magnetic permeability of free space
$\epsilon$	Relative permittivity
$\theta$	Polar angle
$\lambda$	Wavelength
$\mu$	Magnetic permeability
$\phi$	Azimuthal angle
$\Omega$	Angular domain

## LIST OF ACRONYMS/ABBREVIATIONS

AF	Asymmetry Factor
AgNP	Silver Nanoparticle
AR	Aspect Ratio
ATM	Atomic Force Microscope
AuNP	Gold Nanoparticle
DDA	Discrete Dipole Approximation
DDA-SI	Discrete Dipole Approximation with Surface Interaction
DLS	Dynamic Light Scattering
DRS	Diffuse Reflectance Spectrometer
EDX	Energy Dispersive X-ray
EM	Electromagnetic
FDTD	Finite Difference Time Domain
FEM	Finite Element Method
IRIS	Interference Reflectance Imaging Sensor
LSPR	Localized Surface Plasmon Resonance
MAE	Discrete Dipole Approximation
MAPE	Mean Absolute Percentage Error
NP	Nanoparticle
PL	Photoluminescence
PML	Perfectly Matched Layer
POM	Polarized Optical Microscopy
SEM	Scanning Electron Microscopy
SPR	Surface Plasmon Resonance
TEM	Transmission Electron Microscopy
UV-Vis	Ultraviolet-Visible
XPS	X-ray Photoelectron Spectroscopy
XRD	X-ray Powder Diffraction

# 1. INTRODUCTION

## 1.1. Optical Characterization of Nanoparticles

In recent years, the field of nanotechnology, which can be defined as the design, development, and production of nanoscale structures and materials, has expanded rapidly, and its applications are numerous. These applications exist in physics, chemistry, biology, medicine, materials science, and semiconductor manufacturing [1–4]. Due to the fact that the mechanical, chemical, and optical properties of nanoparticles are highly dependent on their size, shape, and composition, nanoparticle structuring permits the manipulation of these properties, hence enabling its application in the aforementioned applications. Changes in size, shape, and materials influence the relative surface area and quantum size effects, resulting in a modification of characteristics [5].

There are numerous types of nanoparticles used for diverse purposes. Considering that bioparticles such as organisms, bacteria, and viruses are also present at the nanoscale alongside nanotechnology, the relevance of identifying nanoparticles increases dramatically. In addition, it is not sufficient to simply detect these nanoparticles; they must also be identified, a difficult task given the nanoscale of these particles. Detecting and characterizing nanoparticles in the aforementioned fields necessitates the development of methods that are relevant, precise, and meaningful.

The nanoparticles can be described in numerous ways, including size, shape, composition, surface charge, and porosity [6]. Various techniques, which can be grouped into four major categories: microscopy-based, spectroscopy-based, X-ray-related, and optical characterization techniques [7], are developed to achieve such characterisation. For nanoparticle characterisation, numerous microscopy-based techniques are applied, such as polarized optical microscopy (POM) [8], scanning electron microscopy (SEM) [9], transmission electron microscopy (TEM) [10], atomic force microscope (AFM) [11] and energy dispersive X-ray (EDX) [12]. Methods based on spectroscopy, such as

ultraviolet-visible spectroscopy (UV-Vis) [13], Raman spectroscopy [14] and Fourier Transform Infrared spectroscopy (FTIR) [15], are commonly employed for analysing the chemical and material-specific properties of nanoparticles. X-ray powder diffraction (XRD) [16] and X-ray photoelectron spectroscopy (XPS) [17] are common X-ray-based techniques for characterisation. Moreover, technologies like dynamic light scattering (DLS) [18], surface plasmon resonance (SPR) based sensors, and interferometric reflectance imaging sensor (IRIS) use optical approaches to analyse NPs.

Optical approaches satisfy the needs of nanoparticle detection and characterization while enabling robust, less expensive implementation. Numerous experimental and computational methodologies have been established to investigate the optical characteristics of nanoparticles in the context of nanoparticle detection and characterization [19]. Nonetheless, these studies may be broken down into two main categories: the detection of nanoparticles on the surface and in suspensions; the majority of techniques can be employed or adapted for each purpose.

Surface plasmon resonance (SPR) is one of the most researched methods for detecting nanoparticles on the surface. It utilizes the oscillation of conduction electrons on the surface of metal nanoparticles to detect NPs [20]. In SPR, the resonance angle of the incident light causes the free surface electrons to resonate due to refractive index difference between the metal film and medium, resulting in a decrease in the intensity of the reflected beam. The position and angle of a black band in the reflected beam provide information about the nanoparticles on the surface. SPR is a well-structured and well-studied technique, although its success with large-scale arrays is restricted.

The Interference Reflectance Imaging Sensor (IRIS) is another recently discovered technology utilized in biomolecular screening applications. It is based on the interference of fields created by sample build-up at the  $Si - SiO_2$  substrate surface [21]. It is a label-free, robust, and rapid method that yields as sensitive data as SPR. It allows for the monitoring of microarrays that permit the simultaneous evaluation of multiple

samples. It also permits dynamic sample monitoring, such as during incubation or replication.

DLS is a method for determining the size distribution of nanoparticles in suspension. In DLS, a monochromatic light source emits a beam of light that impacts the nanoparticles and scatters it in all directions. Since particles in suspension experience Brownian motion, there are fluctuations in the intensity of scattered light. Nanoparticle size can be determined by measuring this intensity of the scattered field in the time domain and using the mathematical link between particle size and time-dependent light scattering.

Typically, these optical techniques utilize the absorption or scattering properties of nanoparticles, or both. Light, which is an electromagnetic (EM) wave, interacts with the particles and can be absorbed or scattered by them. Individual nanoparticles can be recognized based on their optical properties since absorption and scattering can vary dependent on the material, size, shape, and other characteristics of the nanoparticle. Due to weak forces between nanoparticles whose scattering effects may interfere with one another, nanoparticles are typically found in nature as clusters rather than as individual particles. Nevertheless, some of them exist as single nanoparticles, including nano-manufactured particles and bioparticles. Before proceeding with individual nanoparticles, it is crucial to distinguish independent scattering from dependent scattering [22]. Independent scattering indicates that particles are sufficiently separated to absorb and scatter light as if there were no other particles in the nearby [23]. In independent scattering, each particle can be thought to be at a distance from one another. Consequently, these single NPs can be analysed with optical techniques in order to determine their absorption or scattering properties. Absorption and scattering of individual nanoparticles can be solved using the well-known Maxwell equations. There are numerous analytical and numerical methods for solving Maxwell's equations, which will be described in detail in the following sections.

## 1.2. Literature Review

In the previous section, various nanoparticle characterisation approaches were discussed, and it was demonstrated that optical methods are the most prevalent. In addition, it is demonstrated that nanoparticles can be optically treated as single NPs using independent scattering theory, and that their nature can be established by examining their absorption and scattering behaviour. In this section, studies on detection and characterization of nanoparticles are examined, as well as important literature on the use of analytical and numerical approaches in nanoparticle characterization.

Numerous studies examine the impact of NP size on scattering parameters such as scattering cross section, efficiency, and phase function. Using Mie theory, a size analysis is undertaken using multiple databases of silver's refractive index to determine which is most connected with the experimental results [24]. For spherical NPs, a linear association is seen between the size and LSPR peak positions. Observing the surface plasmon resonances of these metallic NPs, Pathak and Sharma studied the absorption and scattering efficiency of many metallic sphere nanoparticles of various sizes in perovskite medium [25]. Perovskite medium has an inverse effect on the scattering efficiencies of nanoparticles, with the peak efficiency decreasing with increasing particle size. In a separate work, the absorption peaks, far-field scattering patterns, and optical band gaps of uranium (U), lead (Pb), cobalt (Co), and thorium (Th) spherical nanoparticles utilized in nuclear security applications with differing particle sizes are studied [26]. The data indicate that the absorption peaks shift to the red when NP size increases. Yang et al. examined numerically the effects of particle size on scattering for spherical, hemispherical, and cylindrical particles on microcrystalline silicon. The near-field intensity of these particles is also examined [27].

Size analysis is conducted not just for spherical NPs, but also for nanoshells and NPs of other shapes. For biosensing, the absorption and scattering cross sections and efficiency of gold nanospheres, nanorods, and silica-gold nanoshells are examined, and a quantitative guide based on Mie scattering and discrete dipole approximation (DDA) is

established [28]. Size study reveals a high correlation between the resonance wavelength of nanoshells and their radius, whilst the resonance wavelength of nanospheres is mostly unaffected by their size. In another study that uses finite element method (FEM) and Mie theory, the size impacts on plasmon resonance for metallic nanoparticles (gold, silver, and copper) are examined, and the results are compared to experimental data [29]. For nanospheres of varying sizes, the extinction efficiencies and peak resonance wavelengths are found, and both increase with increasing size. The cross-section values are also studied with different surrounding media with varying refractive indices, revealing that the change in refractive index of the surrounding medium has a significant impact on the extinction cross section of gold but not silver. AgNP affects the wavelength of the resonance. It is also investigated that the nanoshell thickness resulted in a red shift of plasmonic resonance peaks without significantly affecting the cross-section values.

There are also other analyses which focuses on the shape effects on optical parameters. Mock et al. did an experiment with various sizes and forms (spherical, triangular, and pentagonal) of AgNPs and attempted to identify them based on their surface plasmon resonance. The link between form and plasmon resonances was discovered to be strong [30]. Similar research investigates numerically the LSPR peaks of spherical, nanorod, and bipyramidal AuNPs to characterize these NPs [31]. Compared to nanorods and spheres, bipyramidal nanoparticles exhibit both a high localized sensitivity and a high scattering cross-section. It is also demonstrated that the wavelength of resonance grows as the refractive index of the surrounding medium increases. Ringe et al. examined the impact of size and shape on the normalized scattering of several AuNPs [32]. Regarding their plasmon lengths and side lengths, the efficiencies of the cube, decahedron, icosahedron, triangle, and octahedron are examined.

The impacts of aspect ratio are also explored for gold nanorods and prolate spheroids with variably polarised incident waves, demonstrating that both aspect ratio and polarisation play an important role in the efficiency values and resonance wavelength [29]. Increasing the aspect ratio increases the efficiency and peak wavelength of resonance. In another work, it is demonstrated that the aspect ratio of nanorods

has no effect on the extinction cross section; rather, as the nanorods' effective radius grows, the resonance wavelength changes and the extinction cross section increases [28]. Lee and Sayed studied the effects of AuNPs' size, aspect ratio, and end-cape shape on scattering, absorption, and extinction efficiency with varying refractive indices of surrounding media [33]. Due to their various forms, prolate NPs with the same aspect ratio may have variable scattering efficiencies despite having the same aspect ratio.

To comprehend their nature, the effects of size and shape changes in NP arrays and aggregates on scattering characteristics are also investigated. Using coupled dipole and discrete dipole approximation techniques, the extinction cross section for different one- and two-dimensional AgNP arrays is investigated to analyse the effects of various parameters, such as array perturbations, array orientation change, arrays with coated particles, and arrays in water [34]. The findings of an experiment involving silver nanoparticles are compared to analytical and numerical solutions. Analytical, numerical, and experimental results on the scattering behaviour of AgNPs with varying sizes, media, and interparticle spacing are shown to be in good accord [35].

Using analytical and numerical methods to examine changes in scattering cross sections for arrays of non-absorbent silicon particles, it has been demonstrated that increasing the distance between two sphere nanoparticles reduces the scattering cross section but has no effect on the peak resonance wavelengths. In addition, the formation of arrays increases scattering cross sections [36]. Thiele and French use the finite element approach to predict the scattering characteristics of morphological rutile nanoparticles [37]. In addition, they investigate the scattering of two interacting NPs in both the near-field and far-field, demonstrating that the distance between nanoparticles has a significant effect on their scattering capabilities. The scattering parameter, which is the ratio of scattering cross-section to volume, was observed to rise with increasing nanoparticle distance. Similar research has been conducted to analyse the plasmonic field of gold and silver nanoshell dimers. Analyzing the plasmonic field of nanoshell dimers of gold and silver using multiple expansion and FEM, similar study has been conducted [38]. Liu and Mishchenko studied the optical parameters of soot aggrega-

tion, focusing on the impacts of particle size, fractal size, refractive index, and number of monomers on scattering efficiency and phase function via polar angle [39]. Liu et al. conduct a similar investigation into the effects of water coating on the scattering efficiency and scattering matrix elements of fractal soot aggregates [40].

### 1.3. Objective of the Study

A significant majority of existing research in the literature focuses on the absorption or extinction factors, others examine the scattering effects. The studies that are given in the literature review generally examine the impact of size, arrays and some of them also examine different shapes like nanorods or nanoshells on the plasmonic resonance peaks of particular materials. There are insufficient analyses of shape effects on scattering parameters, specifically the effects of edges on nanoparticles. Moreover, the studies are generally limited to the resonance wavelengths and efficiency values. Even though some analyses focus on the far-field and near-field scattering of the different nanoparticles, scattering matrix elements are rarely examined. This study aims to address these deficiencies by describing AuNPs in terms of size, shape, and aspect ratio by analysing their scattering matrix elements, scattering cross section, and efficiency outcomes. While obtaining a valuable database of the scattering parameters for different nanoparticles, this scattering information enables the definition of the characteristics of differently shaped and sized nanoparticles.

To meet the goals of this study, a finite element model was used to develop that permits the processing of various shapes. The model is confirmed by comparing the findings to analytical solutions for spherical objects, and then simulations are performed for the target nanoparticles, which are spheres, ellipsoids, cubes, and square prisms of varying dimensions. This type of nanoparticle selection allows us to investigate the scattering impacts of various characteristics, including size, shape, aspect ratio, and geometric cross section. To investigate the variation in scattering behaviour caused by adjusting these parameters, a two-step procedure is followed:

- The wavelengths of the plasmonic resonance peaks and their variation as a function of the parameters are determined.
- The first element of the scattering matrix, which is a scaled version of the scattering phase function, is determined at the peak resonance wavelengths where the scattering intensity is highest.

## 2. FORMULATION AND METHOD

### 2.1. Formulation of Light Scattering by a Particle

#### 2.1.1. Electromagnetic Wave in Free Space

The formulation of particle scattering is based on Maxwell's well-known equations, which link the electric and magnetic fields. All calculations for the propagation of electromagnetic (EM) waves and their interactions with matter are derived from Maxwell's equations. Light is accompanied by electric and magnetic fields that oscillate perpendicular to each other and in phase with the wave, which is shown in Figure 2.1. EM waves are attenuated by the mediums that absorb, emit, and disperse them. A perfect dielectric is a material that does not absorb electromagnetic waves. In reality, space is the only perfect dielectric, however, air can be approximated as a perfect dielectric with considerable effects at great distances.

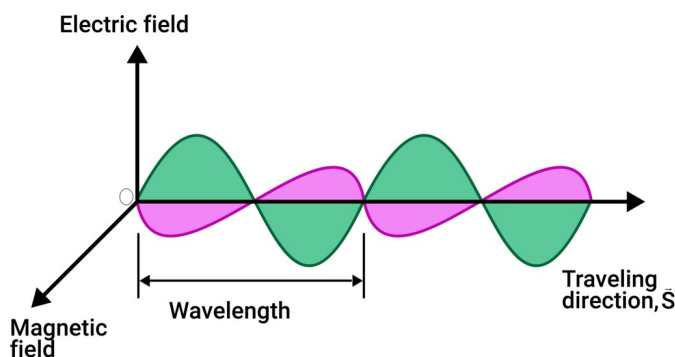


Figure 2.1. Electric and magnetic fields that accompanying EM wave.

The Poynting vector  $\vec{S}$ , defines the EM wave's direction, and its magnitude is equal to the EM wave's energy per unit time and area. It is the cross product of the

vectors for the electric and magnetic fields:

$$\vec{S} = \vec{E} \times \vec{H}, \quad (2.1)$$

where  $\vec{E}$  is the electric field and  $\vec{H}$  is the magnetic field. To determine the magnitude of the Poynting vector, the magnetic field can be described by the electric field:

$$\vec{H} = \frac{\bar{n}}{\mu c_0} \vec{E}, \quad (2.2)$$

where  $\mu$  is the magnetic permeability,  $c_0$  is the speed of light in free space and  $\bar{n}$  is the complex refractive index, which can be written as follows;

$$\bar{n} = n - iK, \quad (2.3)$$

where  $n$  and  $K$  are the respective real and imaginary refractive indices,  $K$  is also called the extinction coefficient. If  $\vec{H}$  in Equation (2.2) is substituted into Equation (2.1), the magnitude of the Poynting vector can be expressed as follows;

$$|S| = \frac{\bar{n}}{\mu c_0} |E|^2. \quad (2.4)$$

For the EM wave propagating in free space, Equation (2.4) can be reduced to

$$|S| = \frac{|E|^2}{Z_0}, \quad (2.5)$$

where  $Z_0$  is the impedance of free space and is the product of magnetic permeability and speed of light in free space:

$$Z_0 = \mu_0 c_0. \quad (2.6)$$

A detailed explanation of the formulation can be found in Howell et al. [41].

### 2.1.2. Scattering Cross Section

Scattering ( $C_s$ ) cross section is important parameter for defining absorption and scattering behaviour. It indicates the effective cross section that the particle scatters and have units of  $m^2$ . Detailed derivation of effective cross section can be found in Bohren and Huffman [42] but can be simply defined as

$$C_s = \frac{1}{I_i} \iint_S \Re(\vec{S} \cdot \vec{n}) dS, \quad (2.7)$$

where  $I_i$  is the incident wave intensity which is defined in Equation (2.5). Dividing the scattering cross section by the geometric cross section perpendicular to the incident wave gives the scattering efficiency

$$Q_s = \frac{C_s}{G}, \quad (2.8)$$

where  $G$  is the geometric cross section.

The Muller matrix relates the scattered and incident Stokes vectors, yields the relationship between intensities at different polarizations. The first element of the scattering matrix  $S_{11}$ , relates the incident intensity and the scattered intensity (magnitude of the Poynting vector);

$$S_{11} = \frac{I_s}{I_i} k^2 r^2, \quad (2.9)$$

where  $I_s$  and  $I_i$  are scattered and incident intensities of the EM wave and  $k$  is the wavenumber defined as follows;

$$k = \frac{2\pi}{\lambda}, \quad (2.10)$$

where  $\lambda$  is the wavelength of the EM wave.  $S_{11}$  can also be related to the scattering cross section:

$$I_s = I_i \frac{1}{r^2} \frac{dC_s}{d\Omega} = I_i \frac{S_{11}}{k^2 r^2}. \quad (2.11)$$

Scattering cross section can be calculated from Equation (2.11) as follows,

$$C_s = \frac{1}{k^2} \int_{\phi=0}^{2\pi} \int_{\theta=0}^{\pi} S_{11} \sin(\theta) d\theta d\phi. \quad (2.12)$$

These equations explain the basics of the EM wave and some basic optical properties that will be used in study.

## 2.2. Finite Element Method for Light Scattering

It has been established briefly that Maxwell's equations can be used to calculate light scattering from particles. Maxwell's equations for light scattering can be solved using a variety of techniques, including Mie and Rayleigh scattering, discrete-dipole approximation, T-matrix, finite difference time domain, and finite element method.

Mie theory is the analytical solution to Maxwell's equations that explains the scattering behaviour of homogeneous spherical objects and also extended for core-shell systems. Mie scattering applies to particles whose diameter is comparable to the incident light's wavelength [43]. Even while Mie scattering provides a precise answer, its application is limited with the spherical objects. Rayleigh scattering is another type of light scattering, specifically elastic scattering by particles with a diameter significantly smaller than wavelength of the incident electromagnetic wave. The Rayleigh-Gans approximation is a method for resolving tiny NPs that employ Rayleigh scattering [44].

There are various ways for calculating absorption and dispersion for increasingly complicated geometries. One of these methods is the discrete-dipole approximation (DDA), which approximates the target shape using a finite array of point dipoles [45]. Discrete-dipole approximation with surface interaction (DDA-SI) was designed to calculate increasingly complex geometries not only in suspension, but also on surfaces [46]. The T-matrix is a computational approach for calculating electromagnetic scattering by single or multiple, nonaxisymmetric, homogeneous NP [47]. The T-matrix approach, also known as the null field method or the extended boundary condition method, is distinguished by its low computational cost and rapid convergence to solutions.

Another numerical method for solving Maxwell's equations is the Finite-Difference Time-Domain (FDTD) method. The domain is partitioned into grids and the time-dependent partial differential equations for electric and magnetic fields are solved using finite differences [48]. Using Fourier transforms, the method can also be employed in a frequency-based fashion, despite its time-based origins. To solve partial differential equations and derive the electric and magnetic field over the domains, the finite element technique (FEM) discretizes the domain into small sections. It is used to frequency domains, and one of its primary benefits is the ability to tackle complex geometries [49]. Given that the Mie solution is restricted to spheres, FEM's ability to cope with all geometries makes it more applicable to real-world issues.

As addressed in the objectives of the study, different shaped and sized nanoparticles will be examined throughout the study, and various methods can be used to solve light scattering problems, which have already been briefly discussed. The finite element method is suitable for studying the interactions between nanoparticles and EM waves because it can work with different shapes and materials of nanoparticles. COMSOL RF (Radio Frequency) module, which is a commercial tool for studying EM wave propagation in high-frequency applications, can be a suitable tool to analyse these nanoparticles. In this section, the implementation of the finite element method is explained. The tool specific details are given in the Appendix A. Throughout the FE model creation, these steps are followed: creation of geometry and boundary conditions of the system, material selection, setting the physics, meshing the geometry, setting the study to analyse the system and obtain the results, and definition of variables that will be used in the derivation of other result.

The first step in the model is creating the geometry of the system. In our case, the nanoparticle is defined in the centre of the model with a specific geometry and size that would change if the particle under study is modified. For the region of free space, a sphere is defined around the nanoparticle with a much larger size. This is the domain around the nanoparticle, and it is defined as a sphere no matter what the particle is. Around this domain, a perfectly matched layer (PML) which absorbs the incident waves and does not reflect anything back into the physical domain to avoid computational errors in the system. PML is an artificial absorbing boundary layer used to limit the computational domain in FEM to increase the efficiency of the method. The generated geometry with nanoparticle, air domain and PML can be seen in Figure 2.2. In this case, the nanoparticle is defined as a sphere, but other nanoparticles such as cube or ellipsoid can be used in other nanoparticle studies.

The material should be assigned to each domain so that the model can use the appropriate optical properties in each domain. The material of the nanoparticles is gold with the optical properties from Rakic et al. 1998: Brendel-Bormann model [50]. The relative permeability is 1 and the relative permittivity can be found in Etchegoin

et al. [51]. The rest of the geometry, domain and PML, is assigned as air, whose relative permittivity and permeability is 1.

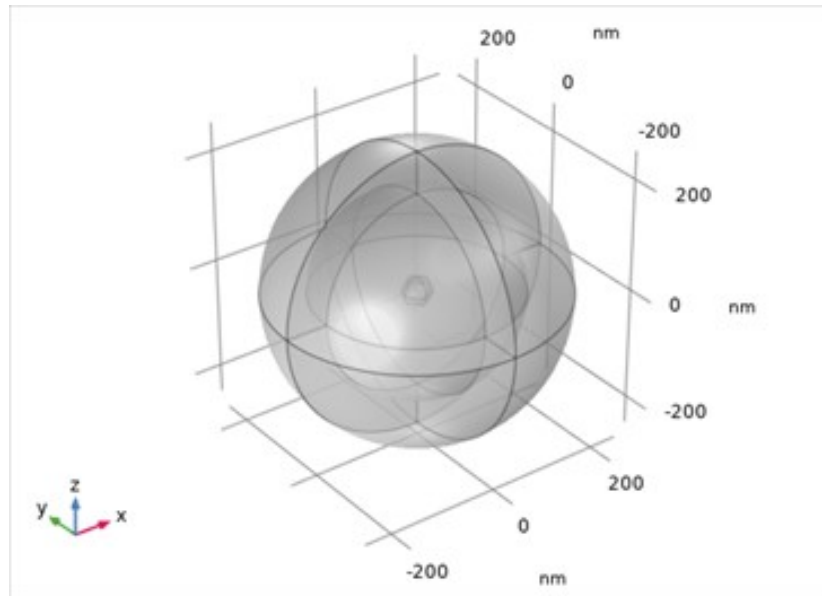


Figure 2.2. Geometry of the model.

The model was created according to physics of electromagnetic waves in frequency domain. A background electric field, whose components are given in Table 2.1, is defined for the incident EM wave of the system. The component or direction is not relevant in the model since the system is symmetric when the nanoparticle is a sphere. For asymmetric nanoparticles, averaging is performed over the orientation, which is explained in detail in Validation and Optimization section. Internal PML surfaces should be provided with scattering boundary conditions and a far-field domain should be defined to calculate the far-field scattering in the geometry.

To perform finite element analysis, all domains should be discretized. The nanoparticle and surrounding empty space are discretized using tetrahedron shaped sub elements. A free triangular mesh is used to mesh the PML domain. However, PML should not be meshed as a single layer. As Grand and Ru demonstrate, a single-layer mesh is insufficient to absorb all outgoing radiation [52]. Therefore, the PML domain can

be divided into a fixed number of elements by sweeping, in our case five. In Figure 2.3, the overall geometry with designated meshes is depicted. The size of the mesh is determined by the geometry and the optical properties desired. Consequently, the selection of the size will be clarified in the Validation and Refinement section.

Table 2.1. Background Electric Field [V/m].

$\mathbf{x}$	$E_0 \exp(-ikz)$
$\mathbf{y}$	0
$\mathbf{z}$	0

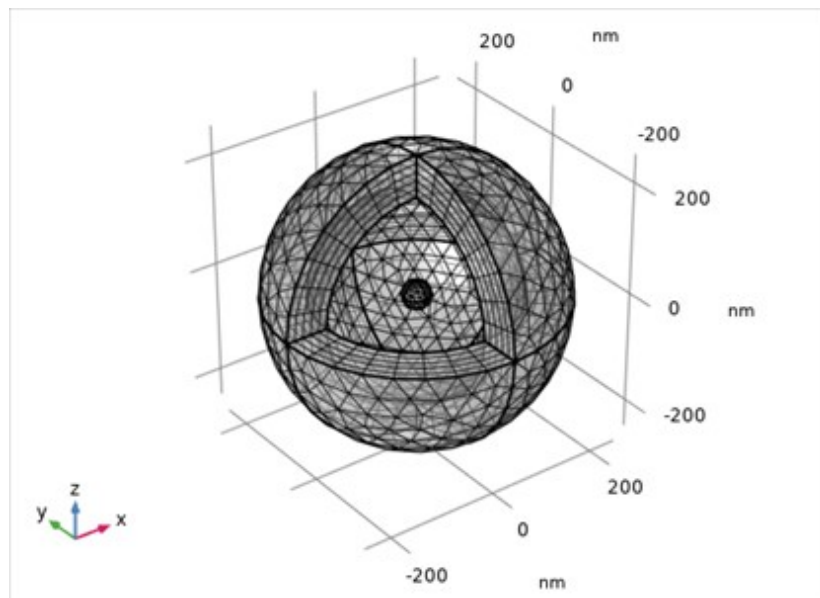


Figure 2.3. Meshing of the geometry.

The next step in the model, before doing the finite element analysis, is the definition of the necessary variables and functions for the model and the desired optical properties. These optical properties are defined, such as the Poynting vector, scattering, absorption, and extinction cross sections, and the corresponding efficiencies, which are listed in Table 2.2, where  $\vec{n}_x$ ,  $\vec{n}_y$ ,  $\vec{n}_z$  are normal vectors and  $\vec{S}_x$ ,  $\vec{S}_y$ ,  $\vec{S}_z$  are components of the time-averaged Poynting vector of the scattered field.  $\int_S$  is the surface

integral of nanoparticle. The analysis results give the Poynting vector of the scattered wave and parametric analysis for different wavelengths, starting at 300 nm and goes up to 800 nm with 10 nm steps, is carried out for optical properties.

Table 2.2. Variables definition for results.

Name	Expression	Unit	Description
$\vec{S}$	$n_x \vec{S}_x + n_y \vec{S}_y + n_z \vec{S}_z$	W/m <sup>2</sup>	Poynting vector
$C_s$	$(\int_S S)/S_i$	m <sup>2</sup>	Scattering cross section
$Q_s$	$C_s/G$		Scattering efficiency

The scattering cross section and efficiency are defined in Table 2.2, which are calculated from the resulting Poynting vector. Existing results can also be used to derive the  $S_{11}$  values at certain wavelengths. Figure 2.4 depicts how a Parameterized Surface is initially defined on the inner surface of PML. Table 2.3 lists the parameters and expressions to define a point in the cartesian coordinates in terms of spherical coordinates, where  $r$  is the radius of the parameterized surface,  $\theta$  and  $\phi$  are the parameters of the surface in spherical coordinates; the former has a minimum of 0 and a maximum of  $\pi$  and the latter has 0 and  $2\pi$ , respectively, and both have discretized into 100 elements. Once the surface is defined, the  $S_{11}$  values can be obtained by using Equation (2.9) on the surface, which gives the formulation of  $S_{11}$  values from the incident and scattering intensities.

Table 2.3. Expressions for the parameterized surface.

$\mathbf{x}$	$r \cos(\theta) \sin(\phi)$
$\mathbf{y}$	$r \sin(\theta) \sin(\phi)$
$\mathbf{z}$	$r \cos(\phi)$

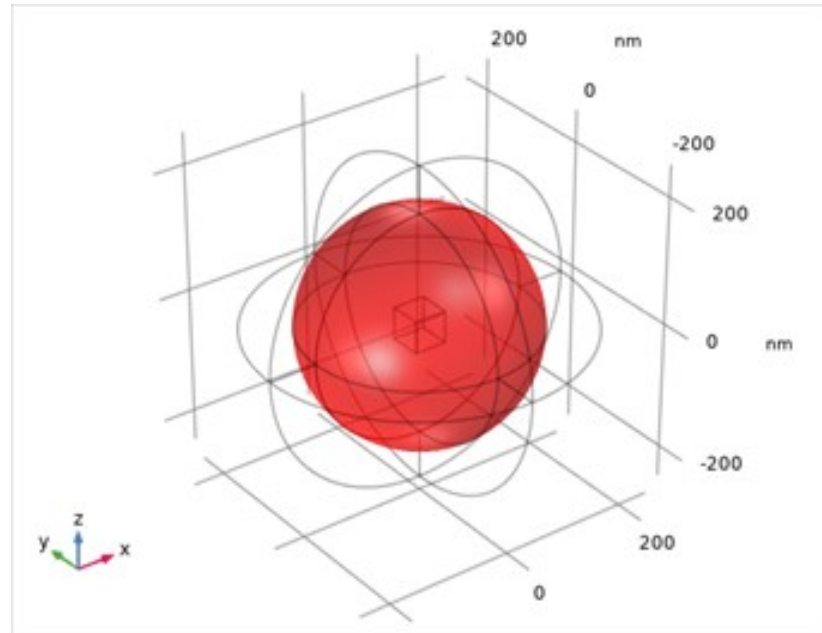


Figure 2.4. The parameterized surface.

MATLAB is used to post-process the exported data in text files. The text files are read using script, the Cartesian coordinates are converted to spherical coordinates, and the data undergoes all post-processing. The results of the absorption and scattering efficiencies are also processed which are explained in detail in the Validation and Refinement section, and MATLAB is used to generate all the graphs in the subsequent sections.

### 2.3. Problem Statement

To investigate the objectives stated in the Objective of the Study section, AuNPs were made with different shapes and sizes, which can be seen in Figure 2.5. A sphere, a cube, three ellipsoids, four cylinders and three square prisms were created, each with size defined by the diameter of the sphere ( $D$ ) and the aspect ratio (see Table 2.4). The  $D$  values were given as 50 nm, 60 nm, 70 nm and 80 nm. The scattering efficiency over a wavelength range from 300 nm to 800 nm and  $S_{11}$  over the polar angle are investigated for each particle to understand the effects of:

- Edges and corners of prisms and cylinders.
- Aspect ratios of ellipsoids, cylinders and square prisms.
- Size changes which affect the volume and cross section area.

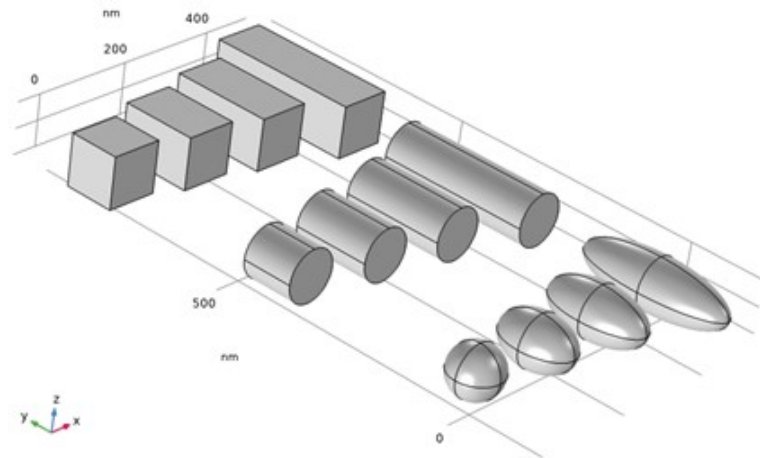


Figure 2.5. Nanoparticles which are investigated throughout this study.

Table 2.4. Dimensions of nanoparticles in terms of diameter of the sphere ( $D$ ).

Nanoparticle	Base Area	Aspect Ratio
Sphere	$\pi D^2/4$	1
Ellipsoid 1.5	$\pi D^2/4$	1.5
Ellipsoid 2	$\pi D^2/4$	2
Ellipsoid 3	$\pi D^2/4$	3
Cylinder 1	$\pi D^2/4$	1
Cylinder 1.5	$\pi D^2/4$	1.5
Cylinder 2	$\pi D^2/4$	2
Cylinder 3	$\pi D^2/4$	3
Cube	$D^2$	1
Square Prism 1.5	$D^2$	1.5
Square Prism 2	$D^2$	2
Square Prism 3	$D^2$	3

### 3. VALIDATION AND REFINEMENT

#### 3.1. Validation and Mesh Refinement of Spherical Objects

##### 3.1.1. Validation and Mesh Refinement for Efficiency Calculations

In FEM, results may vary depending on the number of mesh elements, and the optimal number of meshes and mesh sizes with a reasonable computational effort must be determined to obtain a correct result. Therefore, a mesh analysis is performed for 50 nm and 200 nm gold nanoparticles to determine the optimal mesh size in terms of the correctness of the results and the corresponding computation time. The absorption and scattering efficiencies are calculated for different mesh sizes and the results are compared in the following plots. The mesh sizes are the built-in options of COMSOL itself and the mesh sizes and corresponding mesh elements are given in Table 3.1 for the NPs that studied through this mesh refinement analysis.

Figure 3.1 shows the scattering efficiency of 50 nm AuNP for the different mesh sizes. The results are compared with those of Loke et al. [53]. Only one result is plotted because the Mie and FEM results are almost identical. As can be seen from the graphs, the result converges to reference values when finer grid resolution is used.

Table 3.1. Number of mesh elements for each mesh sizes for denoted NPs.

	Sphere	Cube	Ellipsoid, AR=3
Extra Coarse	1956	-	-
Coarser	3781	-	-
Coarse	7204	-	-
Normal	12705	10693	15717
Fine	20426	-	27023
Finer	48117	45012	57981
Extra Fine	139848	133654	-
Extremely Fine with corner refinement 0.35	-	601758	-
Extremely Fine with corner refinement 0.25	-	626160	-

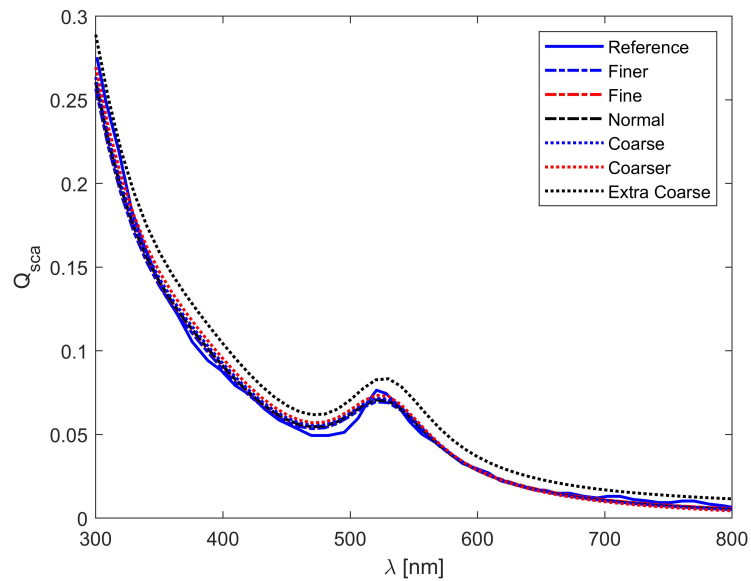


Figure 3.1. Scattering efficiency of 50 nm AuNP.

Figure 3.2 shows the computation time required for simulations and corresponding mean absolute errors (MAE) using different grid resolutions. Each point is given for the mesh sizes built into COMSOL and as expected, the computation time increases as the mesh becomes finer. There is a large jump in time for a finer mesh. Figure 3.2 also shows the mean absolute errors for each mesh size. If we consider both computation time and errors, it would not make sense to choose a finer mesh based on computation time. A normal mesh would be sufficient if the results of the absorption and scattering efficiencies are in one wavelength range, and even a coarse mesh can be considered for 50 nm AuNP due to its lower computation time and reasonably accurate results. All of the simulations are run on the Intel i7-7700HQ with 2.8 GHz processor and 4 cores, all of which are utilized.

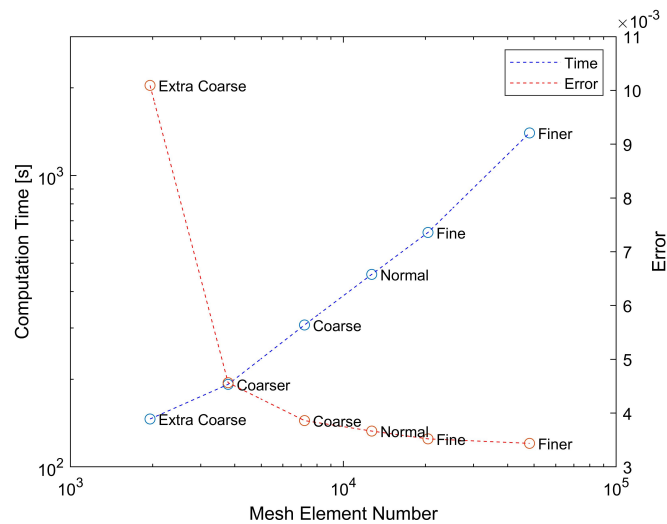


Figure 3.2. Computation time and MAE of 50 nm AuNP for different mesh sizes.

In Figure 3.3, a similar comparison is made for 200 nm AuNP by revisiting the scattering efficiency to validate the model for larger objects, which is also studied in Loke's work. Only normal, fine, and finer meshes are considered, as coarse meshes are not sufficient for this system to converge to results. The results are remarkably similar to one another and to those determined by Loke et al. [53]. Only the analysis results with normal mesh deviate slightly at the lower wavelengths.

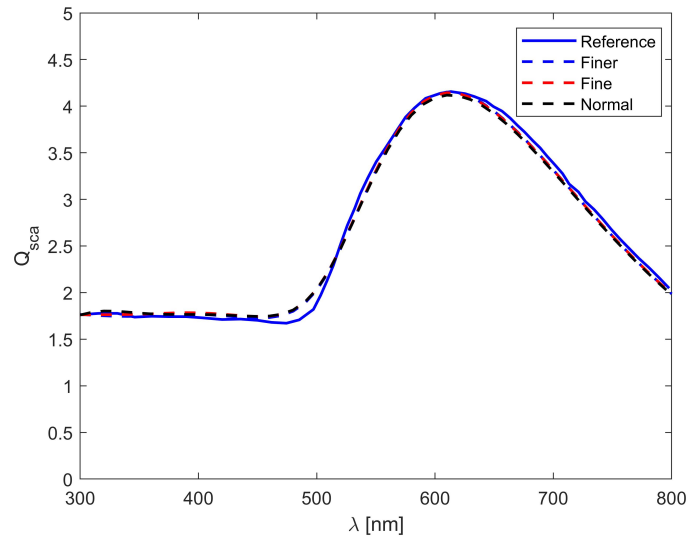


Figure 3.3. Scattering efficiency of 200 nm AuNP.

Figure 3.4 shows the computation time of 200 nm AuNP for the number of mesh elements and the mean absolute errors (MAE) for each mesh size. The finer the mesh, the more computation time is required. Normal and fine meshes require almost the same time for analysis and a fine mesh gives better results in terms of mean absolute error.

In summary, a fine mesh is the optimal mesh size for this system for calculating absorption and scattering efficiencies because it provides accurate results for both small and larger particles and requires lower computational effort. A normal mesh is also an option for smaller particles, as it has similar errors to a fine mesh and requires less time than a fine mesh.

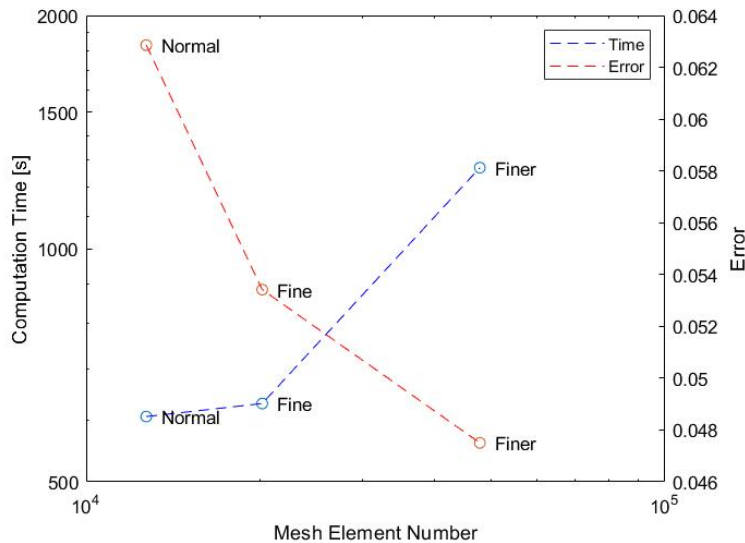


Figure 3.4. Computation time and MAE of 200 nm AuNP for different mesh sizes.

### 3.1.2. Validation and Mesh Refinement for $S_{11}$ Calculations

After determining the fine mesh sizes to obtain results for the scattering efficiency calculation, another mesh analysis is performed for the  $S_{11}$  calculation of 50 nm diameter AuNP for the selected incident wavelength 550 nm. The convergence and accuracy of the  $S_{11}$  results are investigated by this analysis. Figure 3.5 shows the  $S_{11}$  results calculated for different mesh sizes versus polar angle, which are integrated over the azimuth angle. The results are compared with the analytical Mie solution, the results of which are obtained from Philip Laven's MiePlot computer program [54]. The consistency of the results with the Mie solution also proves the accuracy of the COMSOL model created. As expected, the results converge to the Mie solution when finer mesh resolution is used.

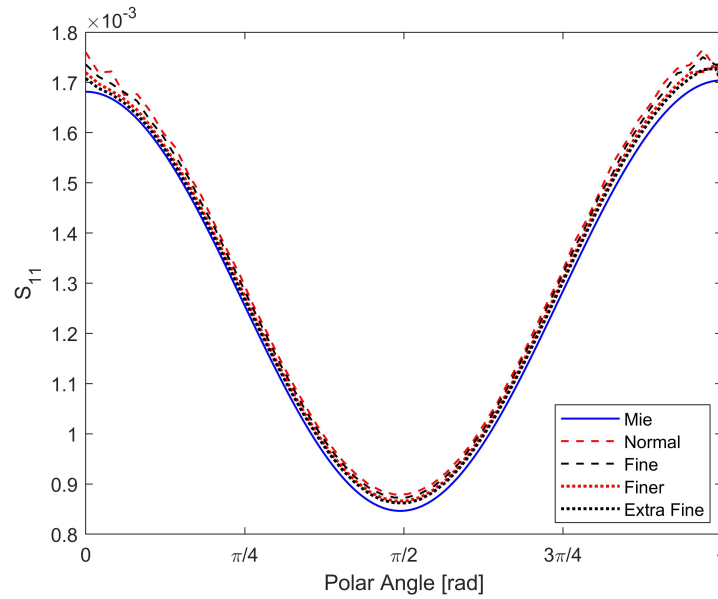


Figure 3.5.  $S_{11}$  through the polar angle for different mesh sizes of 50 nm AuNP.

Figure 3.6 shows the computation time as a function of the number of mesh elements, and the errors are calculated for each mesh size. The calculation time increases dramatically as the mesh size becomes finer to extra fine, but the errors do not decrease at the same rate. A finer mesh also leads to better and smoother results at polar angles close to 0 and  $\pi$ , which do not increase the computation time significantly and where a large decrease in errors is observed. Therefore, a finer mesh is chosen for the calculation of  $S_{11}$  values at certain wavelengths.

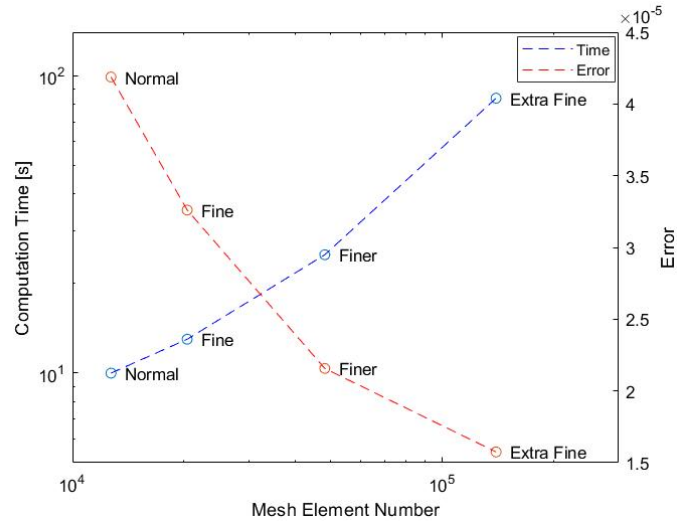


Figure 3.6. Computation time of  $S_{11}$  and MAE of mesh elements of 50 nm AuNP for different mesh sizes.

A similar analysis is performed for 100 nm AuNP to compare finer mesh results with Mie results and to check accuracy at different NP sizes. The comparison of the  $S_{11}$  values for the 100 nm particle with the Mie solution is shown in Figure 3.7. The size independent accuracy of the model is proved by correct results at different particle sizes.

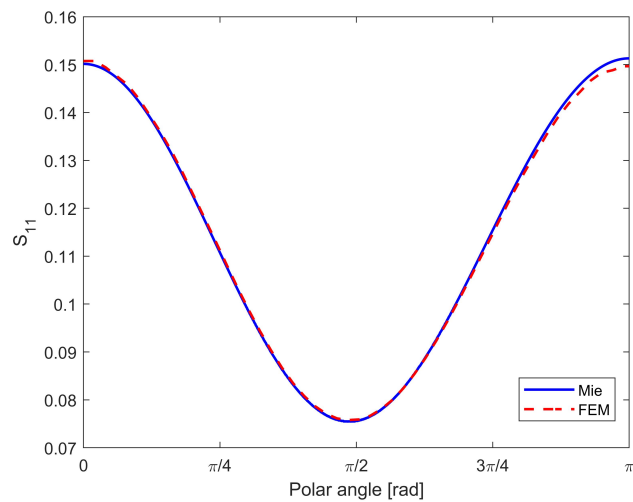


Figure 3.7.  $S_{11}$  through the polar angle at finer mesh size for 100 nm AuNP.

## 3.2. Mesh Refinement and Orientation Averaging of Asymmetric Objects

### 3.2.1. Mesh Refinement of Asymmetric Objects

It is to be expected that the convergence behaviour of other objects which are not continuously symmetric will be different from that of spherical objects. Therefore, a similar process of mesh refinement is performed for other objects: cube and ellipsoid. Figure 3.8 shows the scattering efficiency of an ellipsoid with an aspect ratio of 3 and a diameter of 50 nm for three different mesh sizes: normal, finer, and extra fine. It can be seen that normal or finer meshes have no effect on the scattering efficiency of the ellipsoid.

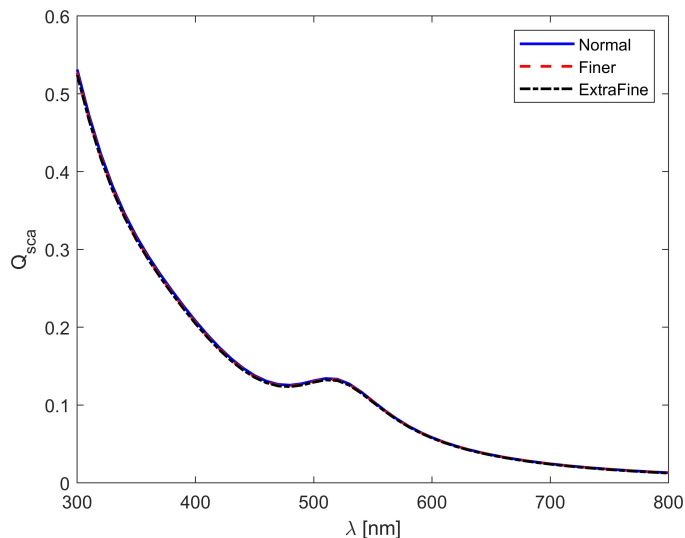


Figure 3.8. Scattering efficiencies of the ellipsoid with different mesh sizes.

A similar analysis is performed for a cube. The scattering efficiency of a cube with an edge of 50 nm is calculated for different mesh sizes. The results are shown in Figure 3.9 and indicate that the built-in mesh options are not sufficient to converge due to the edges and corners of the cube. Therefore, corner mesh refinement is imposed on the cube and the scattering efficiency is calculated with corner refinement scaling of

0.35 and 0.25, the results of which are also shown in Figure 3.9. The difference between uniform mesh and mesh with corner refinement can be seen in Figure 3.10.

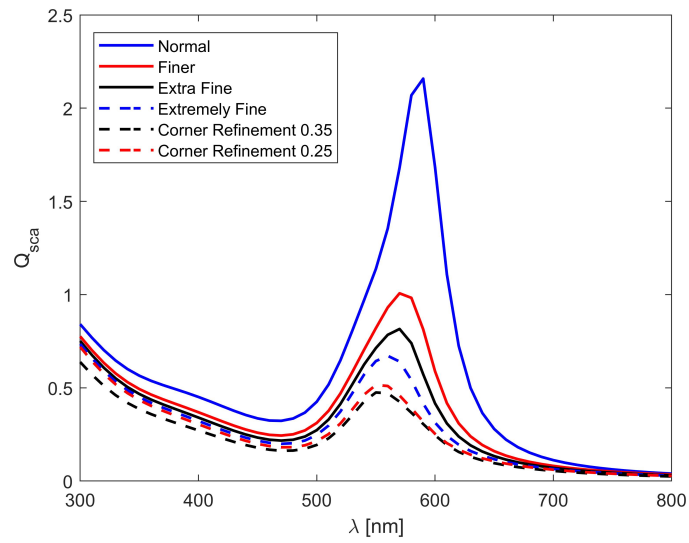


Figure 3.9. Scattering efficiencies of the cube with different mesh sizes and corner refinement.

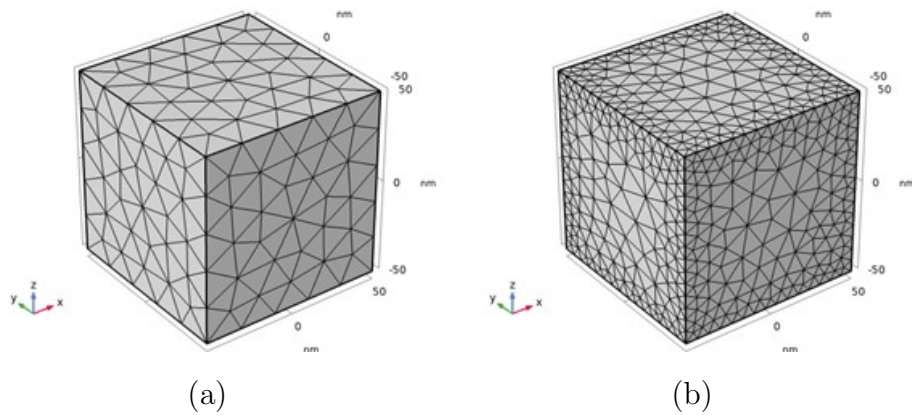


Figure 3.10. Meshing of cube a) with and b) without corner refinement.

### 3.2.2. Orientation Averaging

Typically, nanoparticles do not remain still; they might rotate or vibrate. Consequently, the incident direction of the EM wave would vary with respect to NPs, resulting in different scattering characteristics. Up to this point, all analyses are performed only for a constant incident wave. This is because for spherical objects, a single angle of incidence is sufficient since they are symmetric. However, other objects that are not continuously symmetric would have different scattering behaviour depending on the incident direction of the plane wave. Therefore, the averaging should be calculated over the orientation at different incident angles while keeping the object constant, or the orientation of the object should be rotated with the constant incident wave. The latter was chosen to perform the orientation averaging.

There are different cubature rules for the orientation averaging and grid cubature is followed in this study [55]. The spherical domain around the nanoparticle is divided into grids according to some angle steps and simulations has run for each angle. An example can be seen in Figure 3.11, the direction of EM wave is kept constant according to frame, which is shown in blue arrow in -z direction, and the square prism is rotated around different axis. Some arbitrary orientations of the NP are shown in Figure 3.11.

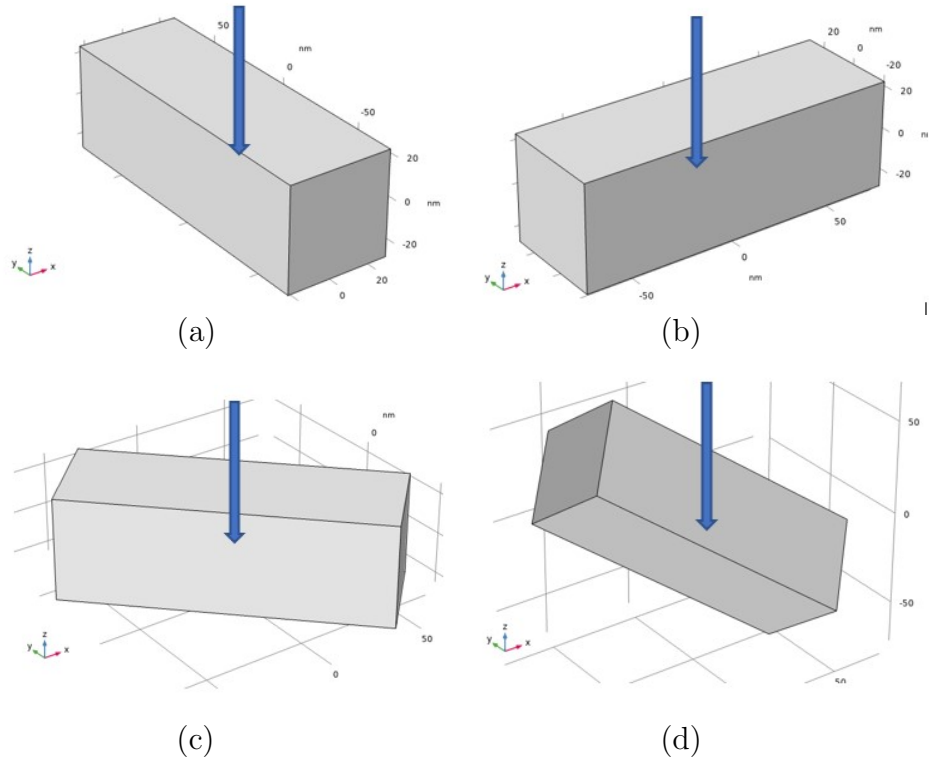


Figure 3.11. Square prism at arbitrary different orientations for orientation averaging at (a) long edge parallel to y axis (b) long edge parallel to x axis (c) long edge rotated  $45^\circ$  around z axis (d) long edge rotated  $45^\circ$  around all axes.

The optical properties can be obtained by integrating and averaging these values around the sphere,

$$f = \frac{1}{4\pi} \int_{\phi=0}^{2\pi} \int_{\theta=0}^{\pi} f(\theta, \phi) \sin\theta \, d\theta \, d\phi, \quad (3.1)$$

where  $f$  is the optical property that would be calculated like scattering cross section or  $S_{11}$ .  $\theta$  and  $\phi$  are the polar angle and azimuthal angle in spherical coordinates respectively. In our case, since the system is discretized, this equation can be written like

$$f = \frac{1}{N} \sum_{n=1}^N f_n, \quad (3.2)$$

where  $f_n$  is the optical property obtained at a given direction and  $N$  is the total number discrete direction. Also, the same procedure can be followed for the geometric cross section. After obtaining the averaged scattering ( $C_{s,avg}$ ) and geometric cross-section ( $G_{avg}$ ) from Equation (3.2), the averaged scattering efficiency can be calculated from Equation (2.8);

$$Q_{s,avg} = \frac{C_{s,avg}}{G_{avg}}. \quad (3.3)$$

A series of simulations is carried out to compare the averaged values and the integrated values. Figure 3.12 shows the scattering cross section values for the ellipsoid with an aspect ratio of 1.5. The integrated values are calculated by taking numerical integral using the trapezoidal rule of the expression given in Equation (3.1). The averaged values are obtained by taking directly statistical mean as in Equation (3.2). As the number of orientations increases, the integrated values and the averaged values converge to the same values. Since the averaged values converge faster than the integrated values, it makes sense to use Equation (3.2) when calculating the orientation averaged values.

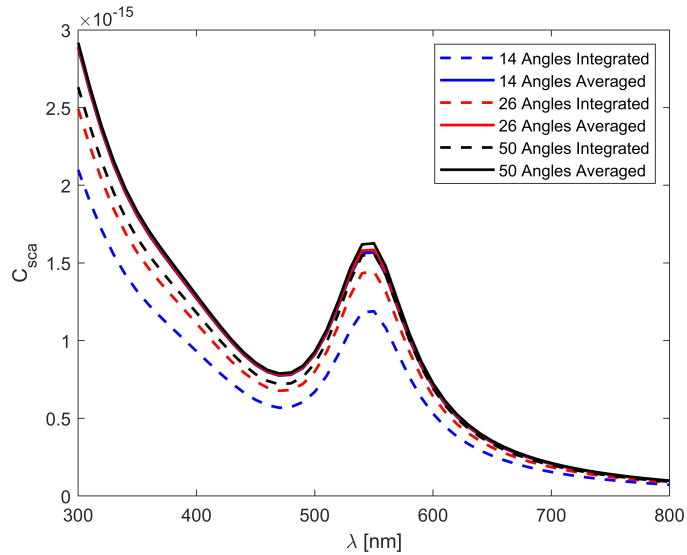


Figure 3.12. Comparison of scattering cross sections calculated averaging and numerical integration.

A cube object with an edge length of 50 nm is created and the  $S_{11}$  values are calculated as the orientation of the cube changes. A different number of directions are taken and the  $S_{11}$  values are compared. For each angle that specified, the NP is rotated around x, y, and z axes only and around both the x and y, x and z, and y and z axes and around the x, y and z axis, which makes 7 different orientations in total for each angle. First, results are obtained with no rotation and then the cube is oriented 45 degrees about the all axis and 14 results are obtained in total and the  $S_{11}$  values are averaged. Then the angle is changed to 30 degrees and rotated around the same axes, planes and space. 21 results are obtained for  $S_{11}$ , which are averaged in the same way. Finally, the orientation degree is decreased to 15 degrees and you get 42 results and the  $S_{11}$  values are averaged which can be seen in Figure 3.13.

There is a clear difference between 14 and 21 different angle-oriented averages of  $S_{11}$ . However, the  $S_{11}$  average of 21 and 42 different angle orientations is almost identical. Therefore, 21 different angles with 30-degree orientation only about the x, y, and z axes and about the xy, xz, and yz axes and the xyz axis would be sufficient for orientation averaging of a 50 nm cube.

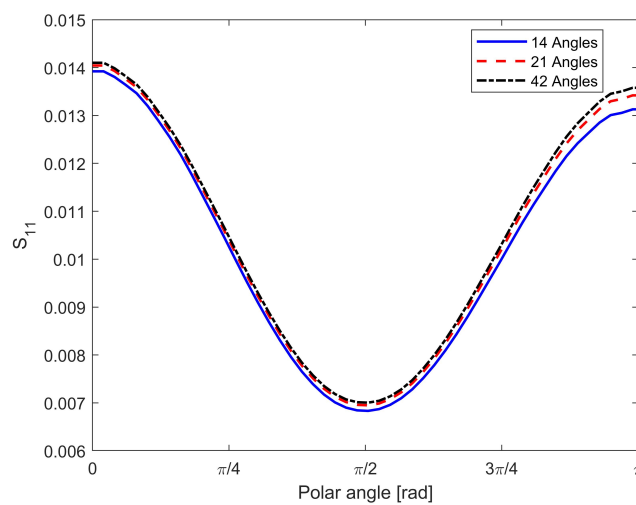


Figure 3.13.  $S_{11}$  by the polar angle with different orientations for cube AuNP whose edge is 50 nm.

A similar analysis is performed for an ellipsoid that has a diameter of 50 nm in two semiaxes and 150 nm in the third semiaxis. Similar angles are chosen, but they are not exactly equal because the ellipsoid is not symmetric when rotated 90 degrees. The results can be seen in Figure 3.14. They do not converge as fast as for the cube since it has fewer axes of symmetry, but 49 angles might be enough to see the behaviour and magnitude of the  $S_{11}$  values.

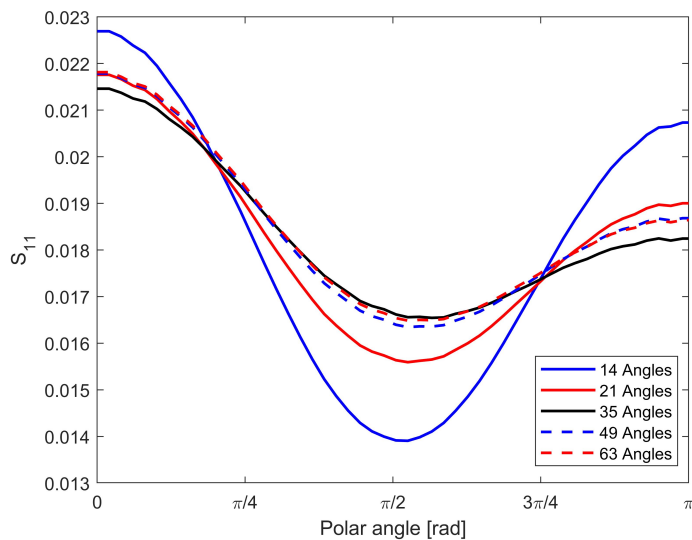


Figure 3.14.  $S_{11}$  through the polar angle with different orientations for ellipsoid AuNP.

These studies show that orientation averaging should be performed over the scattering efficiency calculation of asymmetric objects. The results presented in the following section were calculated in light of the study in this section. In each calculation, the mesh is refined and orientation averaging is performed until the results converge. Table 3.2 gives the necessary number of directions to convergence of results for scattering cross section and  $S_{11}$  calculation. Due to the symmetry of the objects, it is typical for these number directions to be higher. For instance, NP that has not been rotated or NP that has been rotated 180 degrees would result in the same orientation, hence the latter is not considered in the calculation.

Table 3.2. Total number angles needed for convergence of results.

<b>Nanoparticle</b>	$C_s$	$S_{11}$
Sphere	1	1
Ellipsoid 1.5	14	1
Ellipsoid 2	14	35
Ellipsoid 3	14	49
Cylinder 1	14	49
Cylinder 1.5	14	28
Cylinder 2	14	28
Cylinder 3	14	28
Cube	14	21
Square Prism 1.5	14	21
Square Prism 2	14	21
Square Prism 3	14	35

## 4. RESULTS AND DISCUSSIONS

### 4.1. Scattering Efficiency Results

Since this study aims to relate the scattering behaviour of AuNPs to their size and shape, scattering efficiencies are first calculated. Taken into account the analyses in the Validation and Refinement section, the scattering efficiencies are calculated for each particle, which are defined in the problem statement in Figure 2.5 and Table 2.4. Specific mesh sizes are chosen and results are obtained in different orientations until these efficiencies converge to specific results. The averaged geometric cross sections and scattering efficiencies for each particle with different D values (see Table 2.4) are calculated, the former can be seen in Table 4.1.

Table 4.1. Average geometric cross sections in  $[nm^2]$  of NPs for different D values.

Nanoparticle	D=50 nm	D=60 nm	D=70 nm	D=80 nm
Sphere	1963.5	2827.4	3848.5	5026.6
Ellipsoid 1.5	2543.1	3662.1	4984.5	6510.4
Ellipsoid 2	3038.7	4375.7	5955.9	7779.1
Ellipsoid 3	3859.1	5557.1	7563.8	9879.2
Cylinder 1	2581.4	3717.2	5059.5	6608.3
Cylinder 1.5	2938.5	4231.5	5759.5	7522.6
Cylinder 2	3295.7	4745.8	6459.5	8436.9
Cylinder 3	4010.0	5774.3	7859.5	10265.5
Cube	2826.6	4070.3	5540.1	7236.1
Square Prism 1.5	3739.1	5384.3	7328.6	9572.1
Square Prism 2	4406.3	6345.1	8636.3	11280.1
Square Prism 3	5372.4	7736.3	10530.0	13753.5

The scattering efficiencies and the wavelengths at the resonance peaks differ greatly when the particle size and shape change. Due to the fact that these are efficiencies that can be considered scaled, as they are already divided by their geometric cross-sections, they depend less on size effects and more on shape effects. The highest efficiency values at the resonance peaks are listed with the corresponding wavelength of incident light in Table 4.2 and 4.3. These wavelengths are the optimal points for considering the scattering of particles as they have the largest scattering values. The peak positions of the wavelengths are between  $\lambda = 520$  nm and  $\lambda = 770$  nm, while the efficiency values are between 0.069 and 9.634, the latter being more than 100 times larger than the former. This proves that the peak resonance wavelengths and the scattering efficiencies are good indicators for distinguishing nanoparticles. Even though these are the efficiency values, these results show that the wavelength of the resonance peak and the efficiency value increase with increasing size.

Table 4.2. Peak scattering efficiency values at resonance wavelengths.

<b>Nanoparticle</b>	<b>D=50 nm</b>	<b>D=60 nm</b>	<b>D=70 nm</b>	<b>D=80 nm</b>
Sphere	0.069	0.154	0.301	0.537
Ellipsoid 1.5	0.205	0.439	0.768	1.426
Ellipsoid 2	0.863	1.719	2.799	4.031
Ellipsoid 3	6.091	7.267	6.262	5.995
Cylinder 1	0.279	0.564	1.025	1.691
Cylinder 1.5	1.027	2.013	3.111	3.89
Cylinder 2	3.26	5.206	5.876	5.941
Cylinder 3	9.63	9.634	-	-
Cube	0.474	0.979	1.787	2.851
Square Prism 1.5	1.173	2.014	3.101	3.971
Square Prism 2	4.169	4.261	5.123	4.934
Square Prism 3	9.174	7.595	-	-

Table 4.3. Resonance wavelengths of each particle.

Nanoparticle	D=50 nm	D=60 nm	D=70 nm	D=80 nm
Sphere	520	530	530	530
Ellipsoid 1.5	540	550	550	560
Ellipsoid 2	570	580	590	610
Ellipsoid 3	650	670	710	750
Cylinder 1	540	550	550	560
Cylinder 1.5	580	590	600	620
Cylinder 2	620	640	660	700
Cylinder 3	730	770	-	-
Cube	550	560	560	570
Square Prism 1.5	580	590	600	610
Square Prism 2	610	630	660	690
Square Prism 3	720	770	-	-

The scattering efficiency values are obtained for an incident wavelength range from 300 nm to 800 nm. Figure 4.1 and 4.2 show the scattering efficiencies of each shape whose size are different. In each plot, only size effect on scattering efficiencies and resonance wavelength can be observed since the shape and aspect ratio are kept same. In these figures, it can be seen that increase in size cause increase in scattering efficiency values, especially the peak efficiency at lower aspect ratios. However, at higher aspect ratios, which is 3, size increase result in redshift of the resonance wavelength, not affect the peak efficiency value significantly that can be seen in Figure 4.1d, 4.2b and f. Similar phenomenon is observed with cylinder and square prism whose aspect ratios are 2. While the redshift occurs at the resonance wavelengths, efficiencies are only slightly increased, which can be concluded that existence of edges cause this phenomenon at slightly lower aspect ratios, which is shown in Figure 4.2a and e.

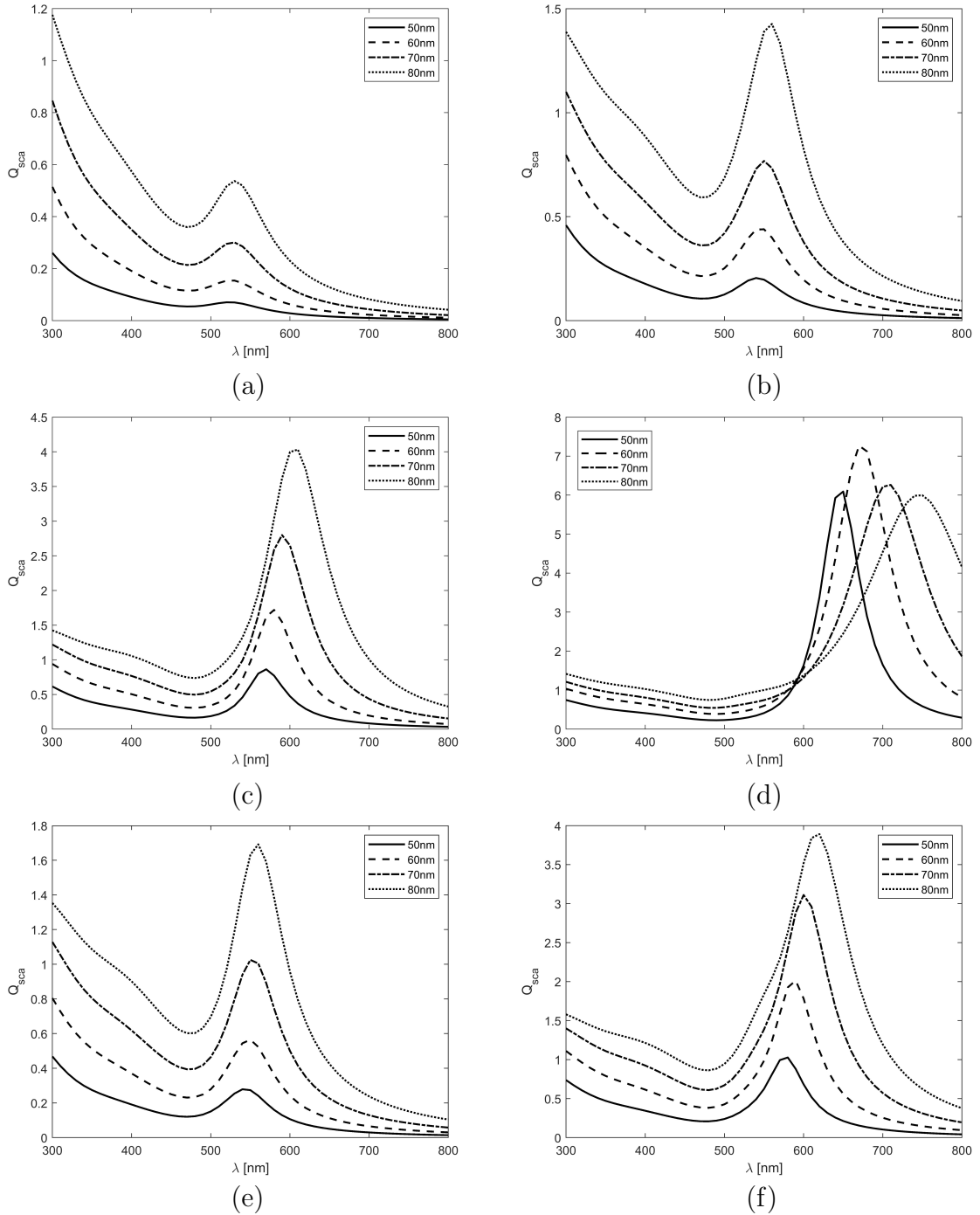


Figure 4.1. Scattering efficiencies over incident wavelength with different sized particles a) sphere b) ellipsoid 1.5 c) ellipsoid 2 d) ellipsoid 3 e) cylinder 1 f) cylinder

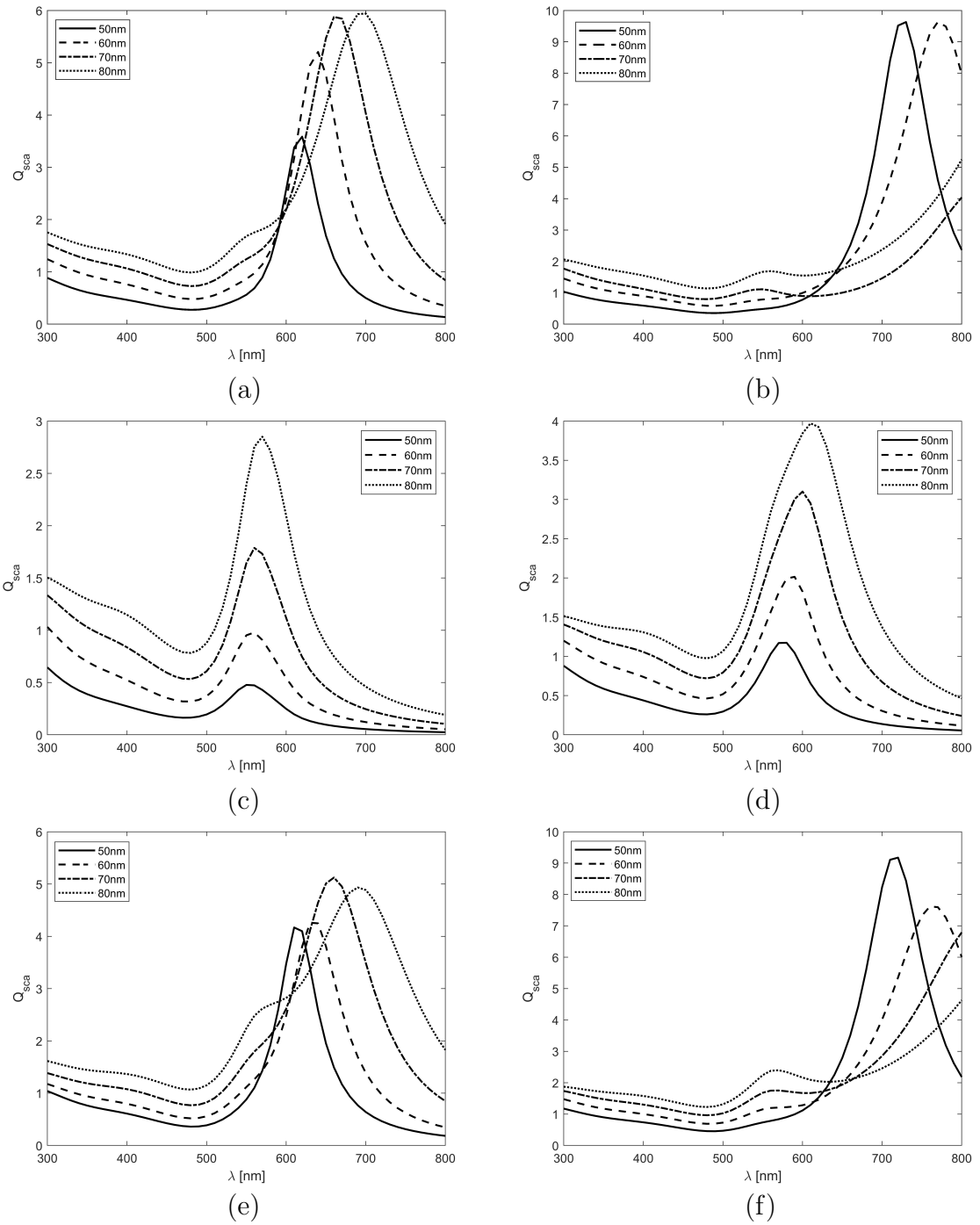


Figure 4.2. Scattering efficiencies over incident wavelength with different sized particles a) cylinder 2 b) cylinder 3 c) cube d) square prism 1.5 e) square prism 2 f) square prism 3.

The scattering efficiency values which demonstrate the size effects for each NP in Figure 4.1 and 4.2, can be also used to compare the aspect ratio and edge effects. Figure 4.3, 4.4 and 4.5 show the aspect ratio effects for particles. In each graph, the shape (existence of edges and corners) and size are kept same so that only aspect ratio effects can be observed. Each of the cases show that increase in aspect ratio results in both redshift of the resonance wavelength and increase in peak scattering efficiency values simultaneously.

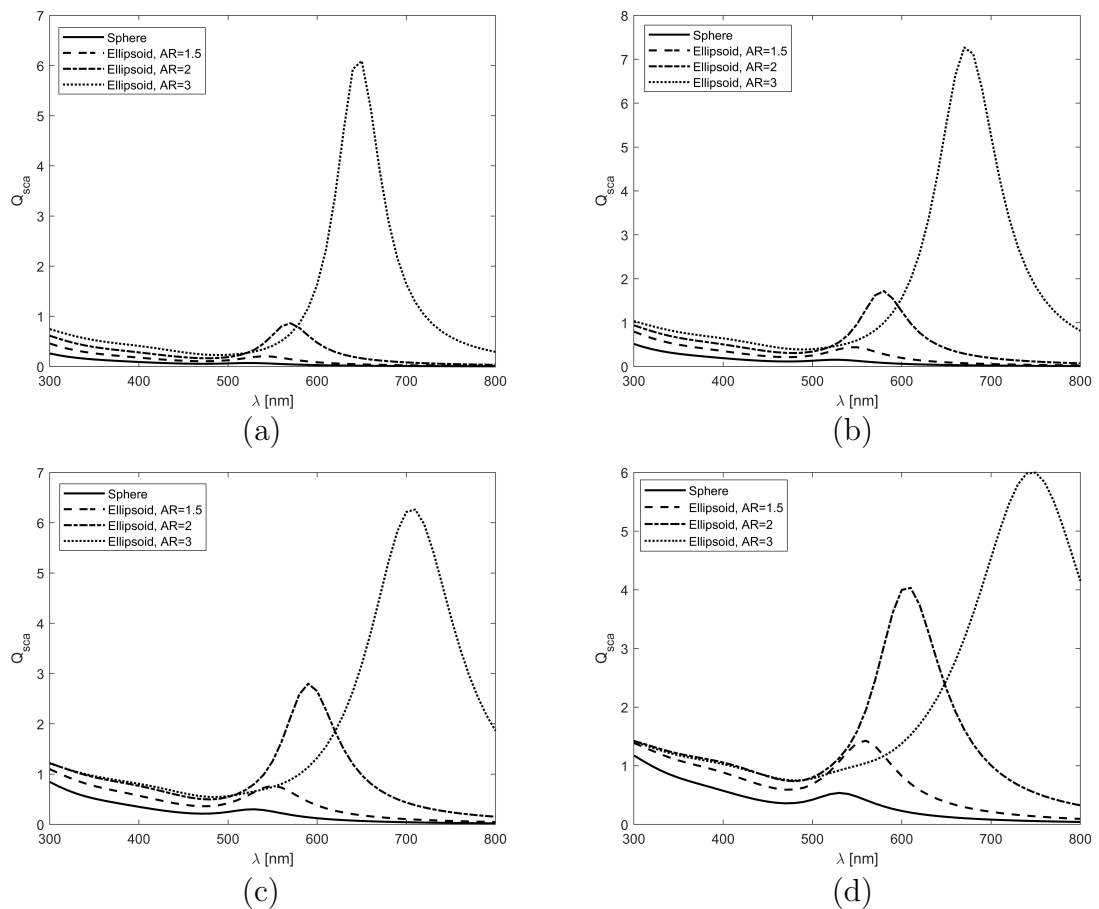


Figure 4.3. Scattering efficiencies over incident wavelength for particles with different aspect ratios a) spheroid 50 nm, b) spheroid 60 nm, c) spheroid 70 nm, d) spheroid 80 nm.

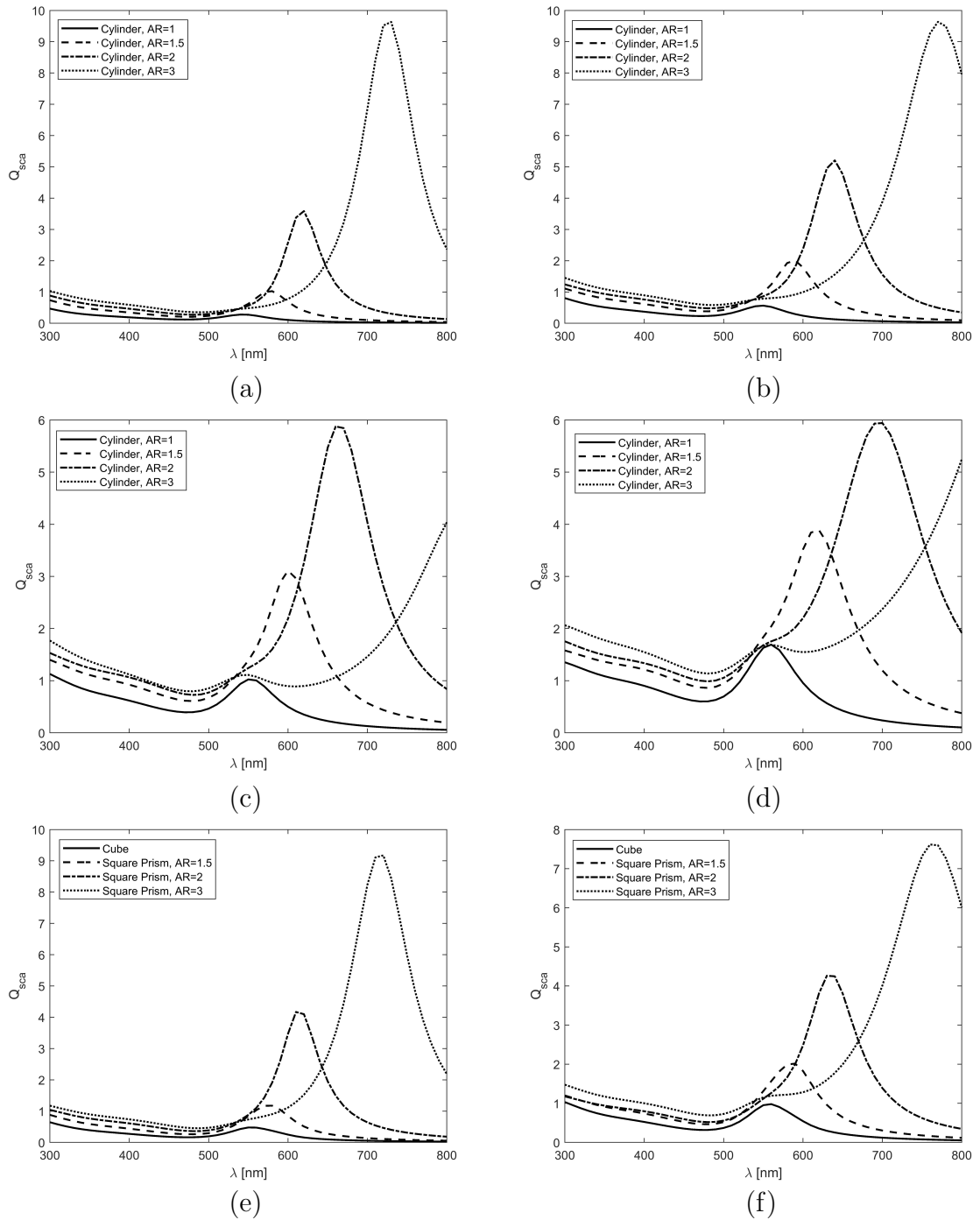


Figure 4.4. Scattering efficiencies over incident wavelength for particles with different aspect ratios a) cylinder 50 nm, b) cylinder 60 nm, c) cylinder 70 nm, d) cylinder 80 nm, e) prism 50 nm, f) prism 60 nm.

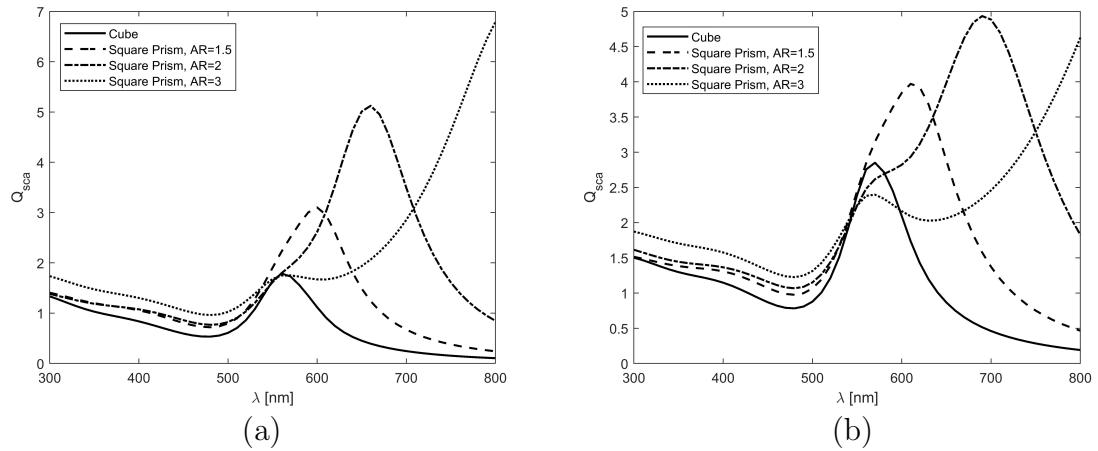
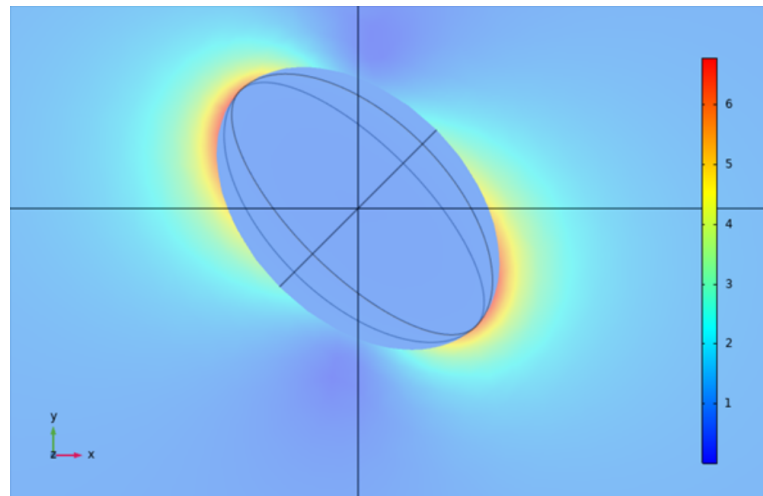
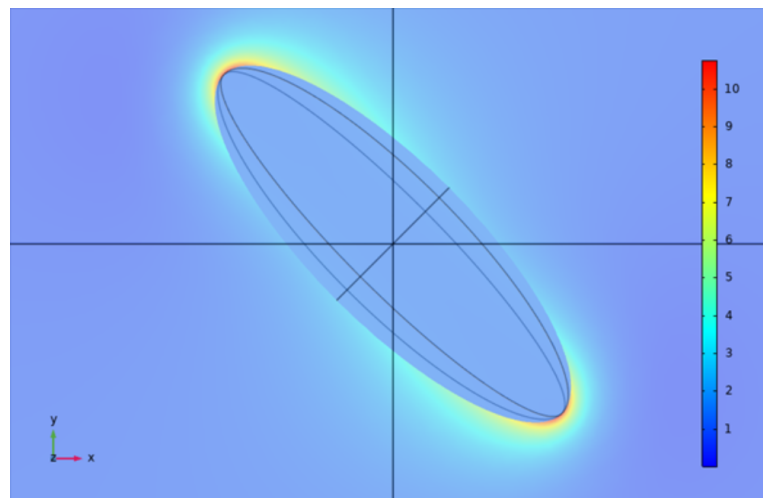


Figure 4.5. Scattering efficiencies over incident wavelength for particles with different aspect ratios a) prism 70 nm, b) prism 80 nm.

In addition to the scattering efficiency values, the electric field distributions around the NPs can be examined to better understand the effects of aspect ratio. Figure 4.6 shows the electric field distribution around two 50 nm ellipsoids with different aspect ratios (1.5 and 3). The electric field distributions are obtained at an orientation angle close to the average value and the incident wavelength of the resonance. It can be seen that the electric field at the tips of the ellipsoid becomes more intense when the aspect ratio is increased. With a lower aspect ratio, when the ellipsoid is closer to the sphere, the electric field is distributed over a larger area of the surface. Increasing aspect ratio causes the sharpening of the tips and these tips behave like corners.



(a)



(b)

Figure 4.6. Electric field distribution around 50 nm a) ellipsoid, AR=1.5 b) ellipsoid AR=3.

After size and aspect ratio effects have been studied and compared, the same results are used to demonstrate the effects of edges. Therefore, particles with similar sizes and aspect ratios are compared to understand only the effects of edges. A sphere is compared to a cylinder with aspect ratio 1 and a cube; ellipsoids are compared to cylinders and square prisms, which have the same aspect ratios. The results are

shown in Figure 4.7, 4.8 and 4.9. The particles with edges, which are cylinders and prisms, have higher peak efficiency values than the particles without edges, which are spheroids. There is also redshift in resonance wavelength, but it is relatively small change when the redshift in aspect ratio is considered. Excepting the comparison at aspect ratio 1, cylinders and prisms have similar efficiency curves. Therefore, it is not possible to detect corners, which exist in prism and not in cylinder, by looking scattering efficiency of these particles.

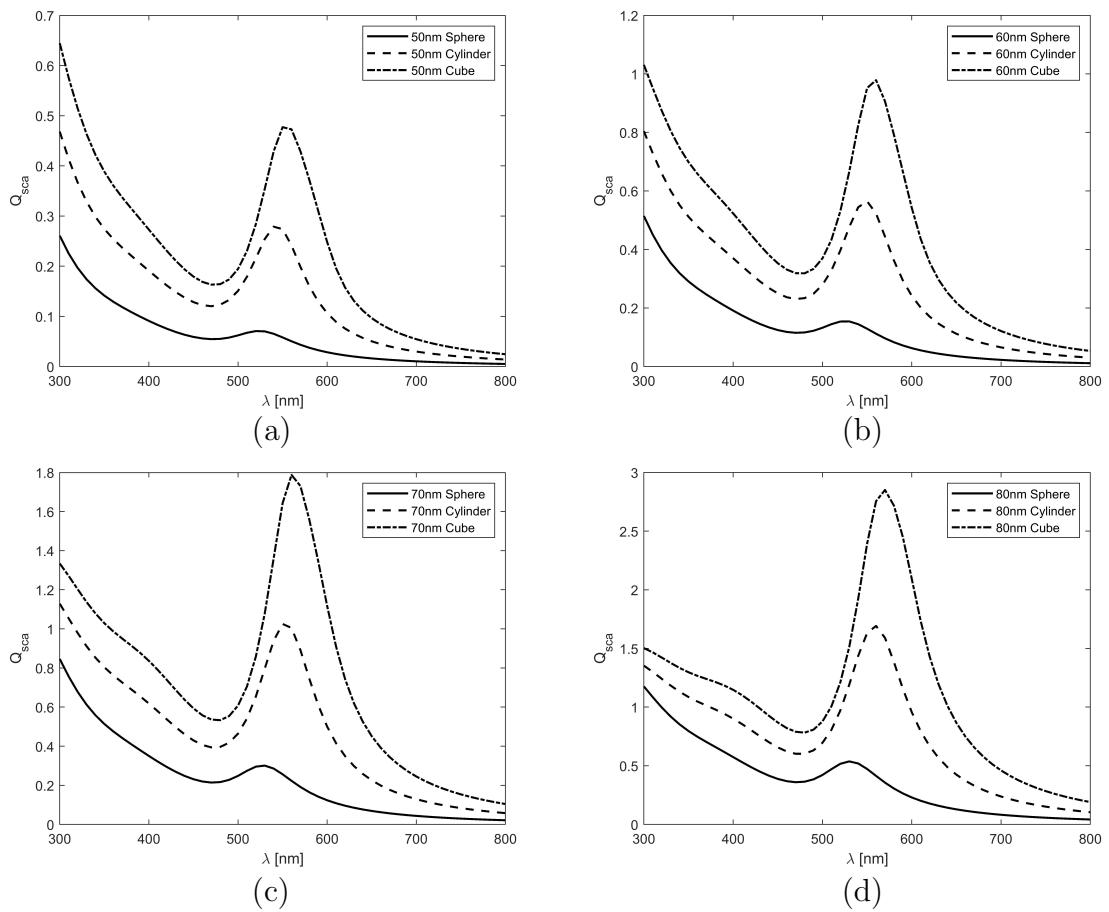


Figure 4.7. Scattering efficiencies over incident wavelength for particles with different edges and corners a) AR1 50 nm b) AR1 60 nm c) AR1 70 nm d) AR1 80 nm.

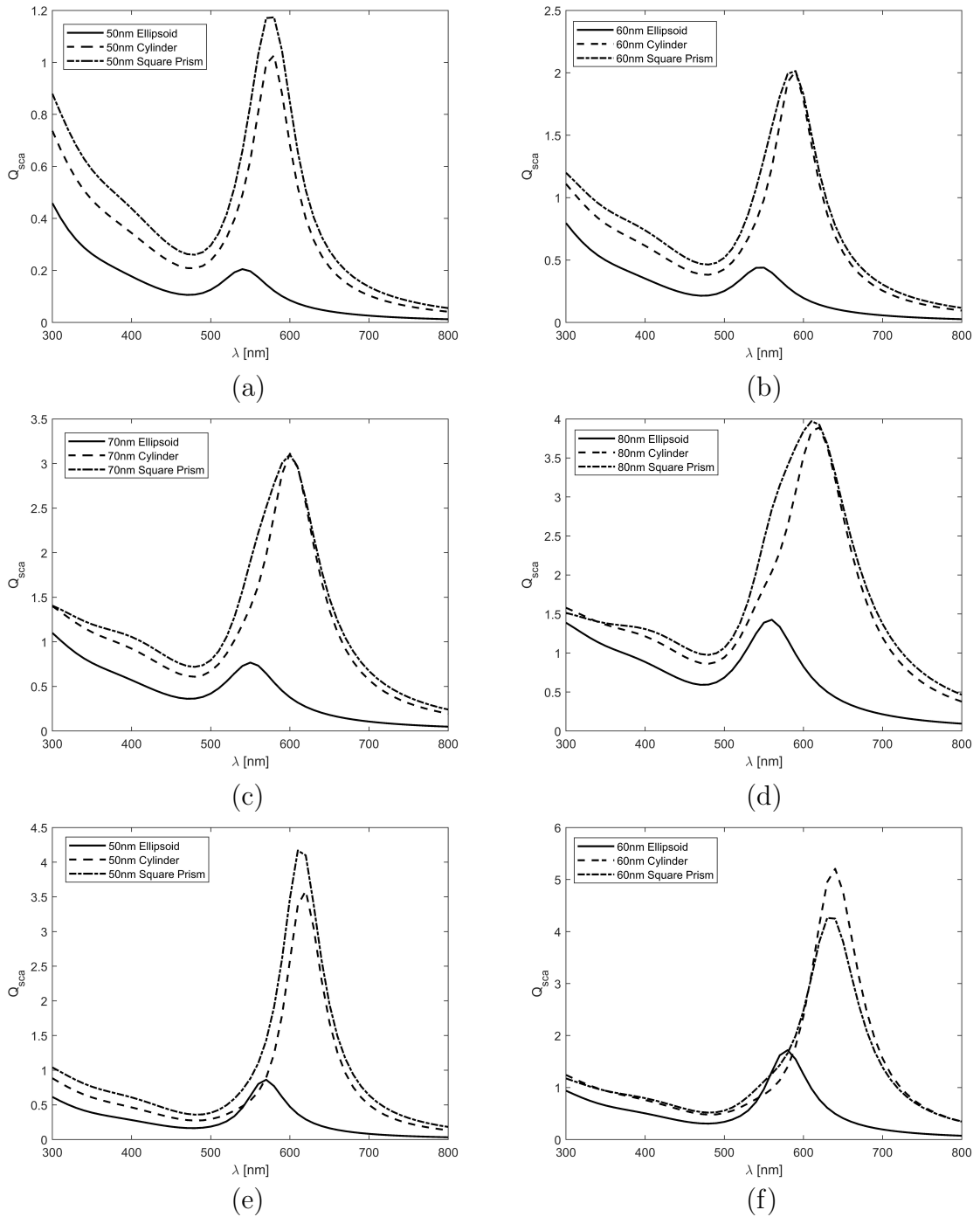


Figure 4.8. Scattering efficiencies over incident wavelength for particles with different edges and corners a) AR1.5 50 nm b) AR1.5 60 nm c) AR1.5 70 nm d) AR1.5 80 nm e) AR2 50 nm f) AR2 60 nm.

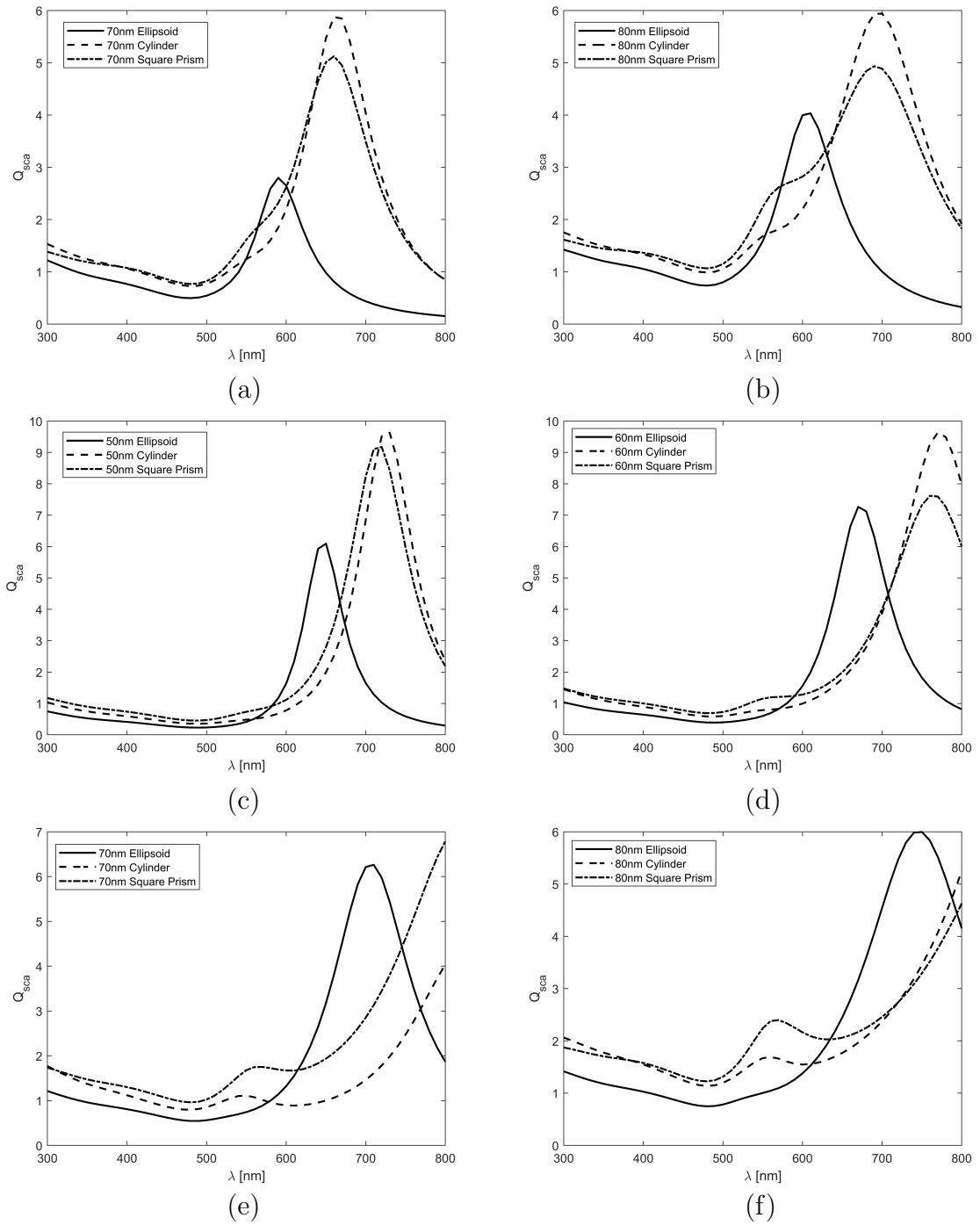


Figure 4.9. Scattering efficiencies over incident wavelength for particles with different edges and corners a) AR2 70 nm b) AR2 80 nm c) AR3 50 nm d) AR3 60 nm e) AR3 70 nm f) AR3 80 nm.

The edge effects can also be observed by examining the electrical field distribution around NPs, like already done for ellipsoid. Figure 4.10, 4.11, 4.12 and 4.13 show the electrical field distribution, which are calculated at corresponding resonance wavelengths, around the cylinder and square prism nanoparticles with aspect ratio 1.5 and 3. As can be seen, electric field intensifies at the corners of NPs, which is the reason of corner effects that have been observed in scattering efficiencies. An aspect ratio comparison can be made by comparing these nanoparticles among themselves. For both cylinder and square prism, electric field values are increased with increasing aspect ratio which is also observed in scattering efficiency curves. It is also possible to make an electric field distribution comparison between the cylinder and square prism since their size and aspect ratio are the same. The electric field intensified at the corners of the prism but in cylinder it is distributed over the cylinder edge. Therefore,  $S_{11}$  values, which are used to examine directional distribution of scattered electric field, can be used to understand the difference between square prism and cylinder. Because this distinction cannot be made by looking only at scattering efficiencies due to similarities which are shown in Figure 4.7, 4.8 and 4.9.

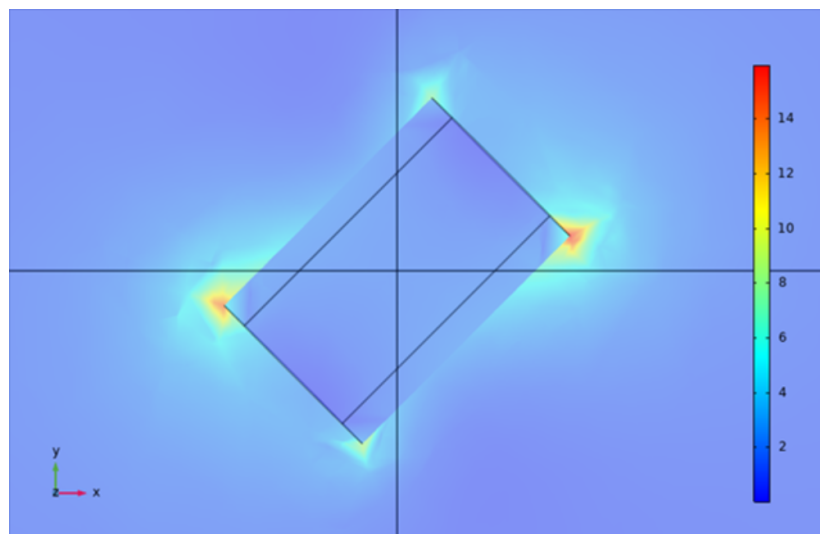


Figure 4.10. Electric field distribution around 50 nm cylinder, AR=1.5.

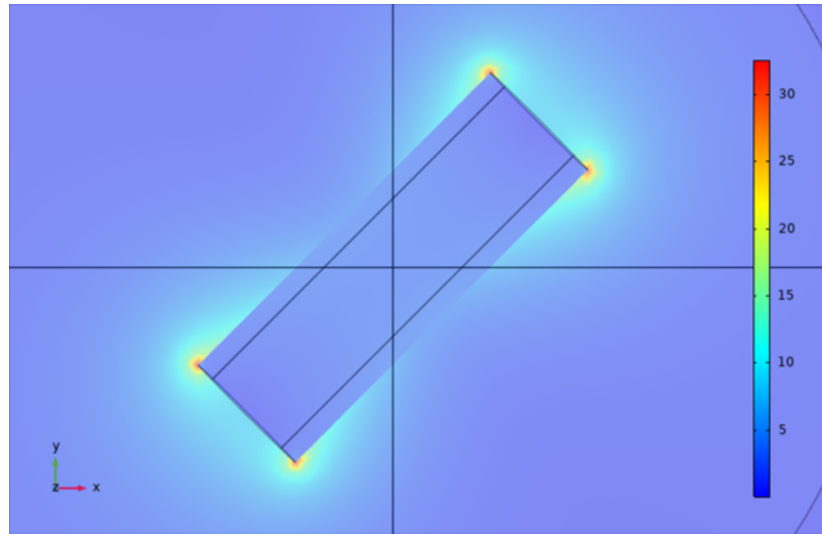


Figure 4.11. Electric field distribution around 50 nm cylinder, AR=3.

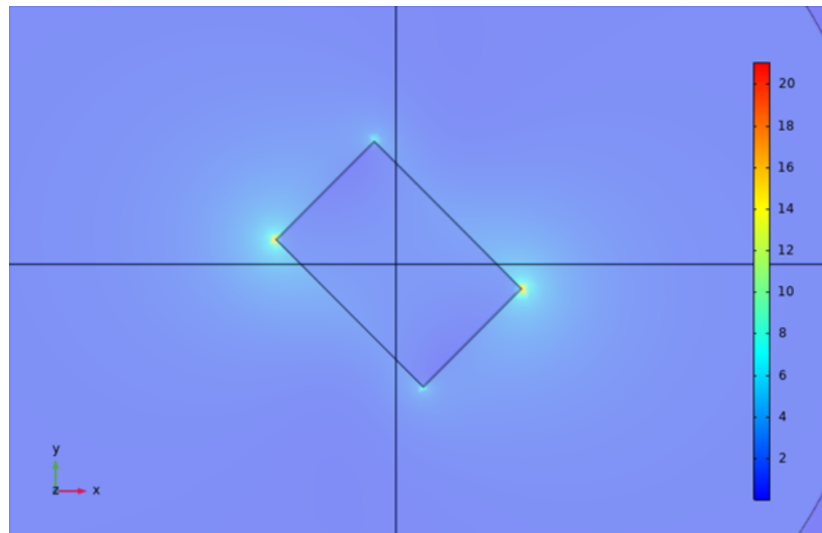
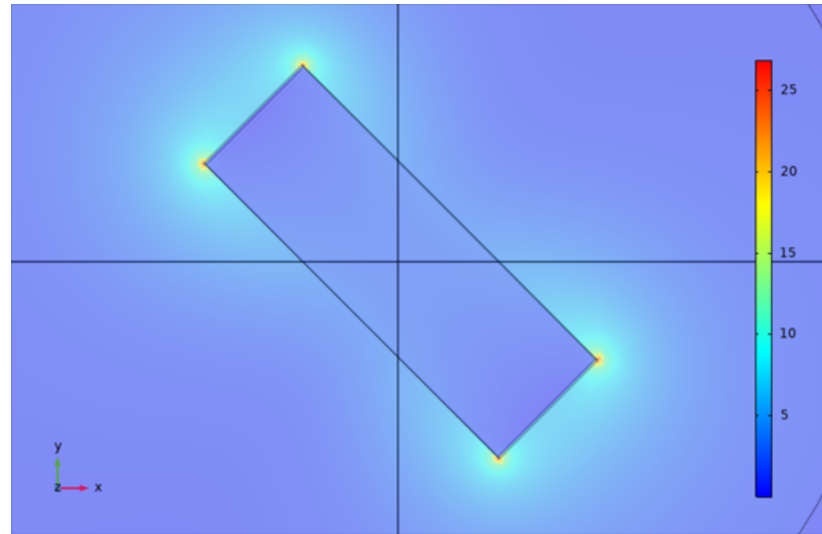


Figure 4.12. Electric field distribution around 50 nm square prism, AR=1.5.



(d)

Figure 4.13. Electric field distribution around 50 nm square prism, AR=3.

Although the particle sizes are defined with the characteristic length parameter  $D$ , the particle cross section areas can be different due to shape changes. In Figure 4.3, 4.4 and Figure 4.7, 4.8, 4.9; the particles with the same characteristic length are compared but cross section areas, which are tabulated in Table 4.1, are different due to edge and aspect ratio differences. To eliminate the effects of difference in cross section area, particles that have the same cross-sectional area are compared with each other to observe effects of only aspect ratio and only edge. Figure 4.14 shows the aspect ratio comparison of the same objects with same cross section areas. Figure 4.14a and b demonstrates that increase in aspect ratio hugely affect the peak efficiency and resonance wavelengths for smaller objects. However, for larger objects such as the particles that are given in Figure 4.14c and d, aspect ratio effects are limited.

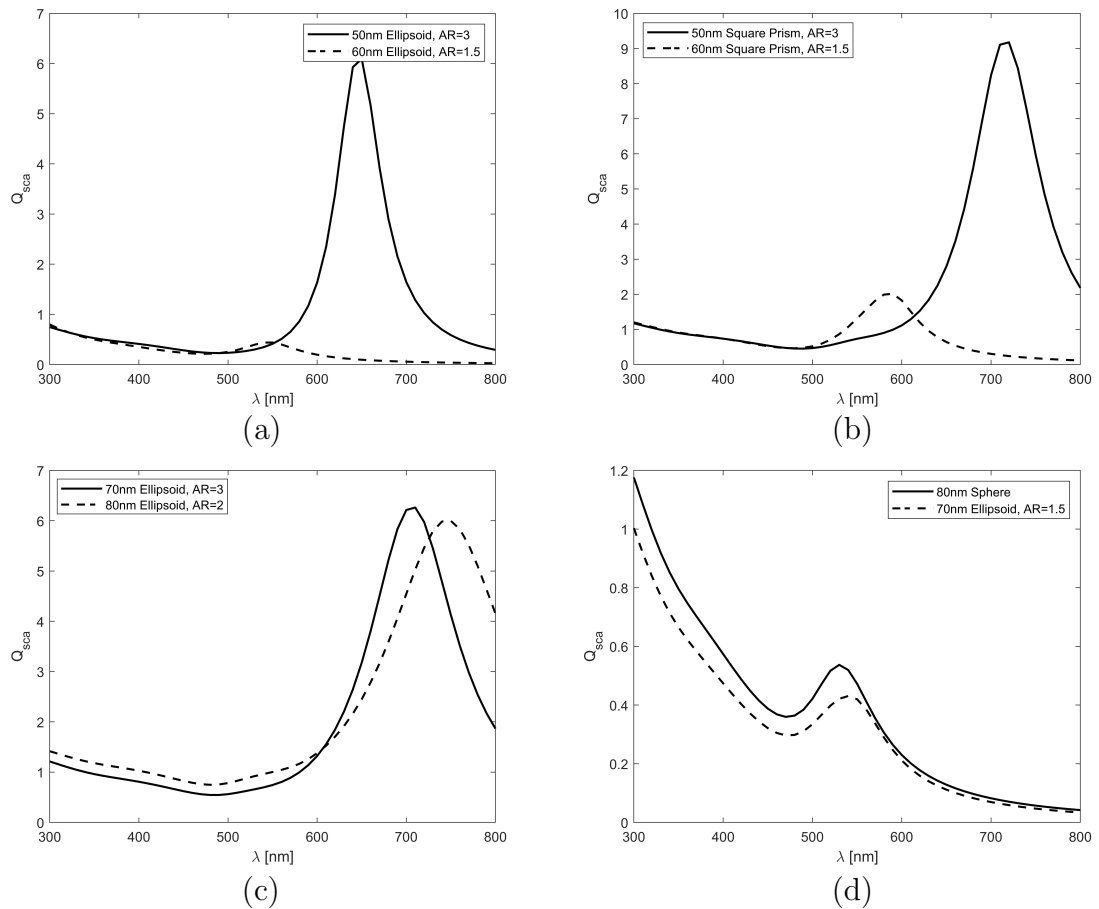


Figure 4.14. Scattering efficiencies over incident wavelength for the particles that have the same shape and cross-sectional area.

A similar comparison is made between spheroids and prisms to see the effects of edges, just by looking at particles that have the same aspect ratio and cross-sectional area. Figure 4.15a shows the comparison between a 50 nm cube and a 60 nm sphere, and Figure 4.15b shows the comparison between a 60 nm ellipsoid and a 50 nm square prism with an aspect ratio of 2. In each case, the edge effects increase the peak efficiency enormously, but do not cause the redshift in resonance wavelength significantly.

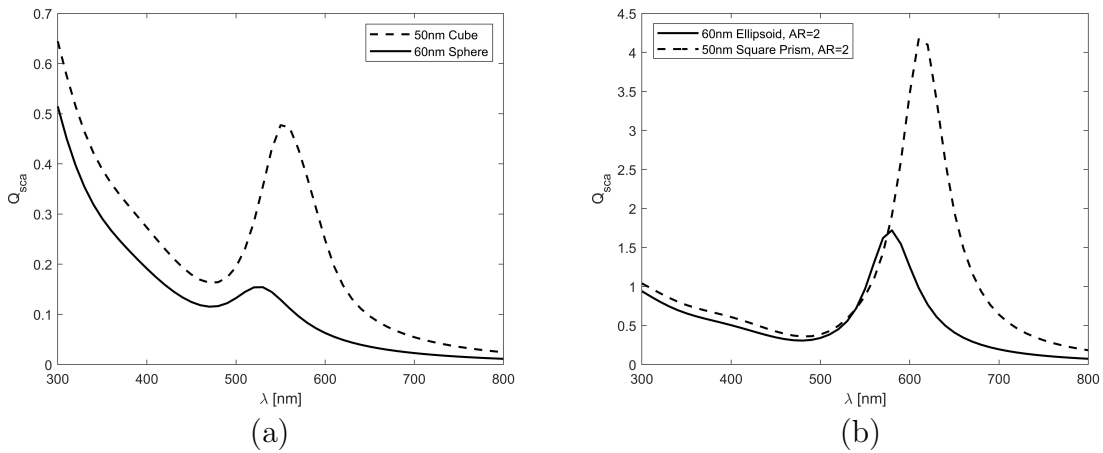


Figure 4.15. Scattering efficiencies over incident wavelength for the particles that have the same aspect ratio and cross-sectional area.

All of the peak efficiency values and corresponding wavelengths are displayed as a scatter plot with respect to aspect ratio. Curve fits are implemented for each shape: spheroid, cylinder and prism. As can be seen in Figure 4.16a, the peak scattering efficiency increases exponentially with increasing aspect ratio for each shape. The efficiency values are higher for cylinders and prisms at every aspect ratio point that proves the effects of edges directly affects the efficiency values. A linear relationship is observed between the aspect ratio and resonance wavelengths which is graphed in Figure 4.16b. Similarly, when the curve fits of the spheroid and edged particles, cylinder and prism, are examined, it is observed that edge effects increase the resonance wavelength for the particles. Another important point is that both efficiency and resonance wavelength curves exhibit matching behaviours. A variability chart is created for examining the peak efficiency and resonance wavelength of the particles, which is given in Appendix B. These variability charts also depict that cylinder and prisms follow the same trend for efficiency and wavelength values. Therefore, the existence of edges can be understood by examining peak efficiency and resonance wavelength values from the difference of spheroid with other. Nevertheless, the existence of corners cannot be observed from peak efficiency and resonance wavelength since the cornered particle

(prism) and the agonic particle (cylinder) cannot be distinguished by examining their peak efficiency and resonance wavelength values. This distinction may be observed by looking at the directional distribution of scattered light, which is examined in the next section with  $S_{11}$  values.

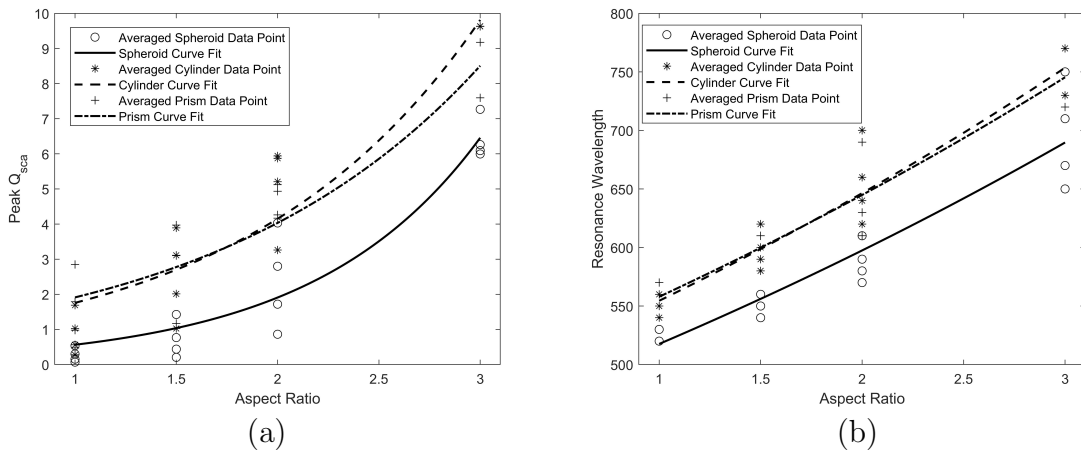


Figure 4.16. Scattering efficiencies over incident wavelength for the particles that have the a) same aspect ratio and b) cross-sectional area.

Up to this point, the scattering efficiencies are demonstrated in a wavelength span and the results have compared each other visually. Statistical analyses are carried out to understand the effects of the parameters to the scattering efficiency and resonance wavelength. Firstly, a regression method is implemented to all dataset through spectral domain. Efficiency values are listed for each incident wavelength, size and shape values. Incident wavelengths change between 300 – 800 nm, size is taken as averaged cross section area and shape is taken as aspect ratio values and edge-corner existence. The edge parameter is defined with three different ways and three different datasets are obtained. Firstly, edge is taken 0 for spheroids, 0.5 for cylinders and 1 for prisms. Secondly, total edge length per surface area is calculated for each particle. Finally, surface area per volume is taken as edge parameter. Total number of 2448 data is split into test and train data and fed into random forest regression model, which utilizes both ensemble learning and decision trees.  $R^2$  scores, mean absolute percentage errors

(MAPE) are listed in Table 4.4. Importance of each parameter is calculated for each dataset and shown in Table 4.5. Scikit-learn library of Python is used to implement random forest regression.

Table 4.4.  $R^2$  and mean absolute percentage errors for each dataset.

	<b>Dataset 1</b>	<b>Dataset 2</b>	<b>Dataset 3</b>
$R^2$ <b>Train Score</b>	0.995	0.996	0.996
$R^2$ <b>Test Score</b>	0.973	0.972	0.969
<b>MAPE %</b>	7.39	7.45	8.19

Table 4.5. Importance of each parameter on scattering efficiency.

<b>Importance (%)</b>	<b>Dataset 1</b>	<b>Dataset 2</b>	<b>Dataset 3</b>
Wavelength	39.8	39.5	40.1
Cross Section Area	35.7	34	33.2
Aspect Ratio	19.3	19.7	19.2
Edge	5.2	6.8	7.5

For each dataset, the  $R^2$  values are very high for both the test and train data. The mean absolute percentage error is also low in each case. The order of importance is the same for each dataset and the percentages differ slightly between the datasets. The wavelength of the incident wave has the greatest influence on the scattering efficiency, as the values are taken for the entire wavelength domain. The wavelength is followed by the cross-section, which has already been shown in the previous diagrams. The aspect ratio also has a significant influence on the scattering efficiency. The edge seems to be less important. However, since the definition of the edge is not clear, there may not be enough breakpoint for the edge parameter to assess the importance of the edge.

As already mentioned, these importance values are calculated for all spectral domains. However, focusing on the resonance wavelength and corresponding efficiency peaks is better way since these points are more characteristic for scattering behaviour

of the particle. Therefore, a sensitivity analysis is conducted by using the peak efficiencies and resonance wavelengths that are given in Table 4.2 and 4.3. Normally in the sensitivity analysis, the increase and decrease ratio of one parameter is kept same while keeping other variables constant so that only the effect of one parameter can be observed with constant increments or decrements. However, due to the large data intervals it is not possible to implement sensitivity analysis in the same manner. Yet, it can still be used to understand effects of parameters to see the most important parameter. In Figure 4.17, the importance of the parameters on the peak scattering efficiency and resonance wavelength are shown.

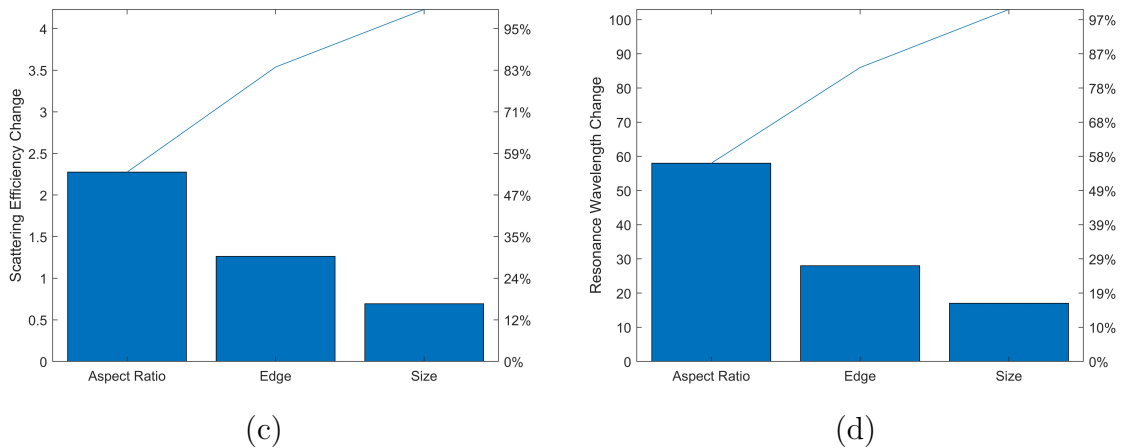


Figure 4.17. The importance parameters on a) peak scattering efficiency b) resonance wavelength.

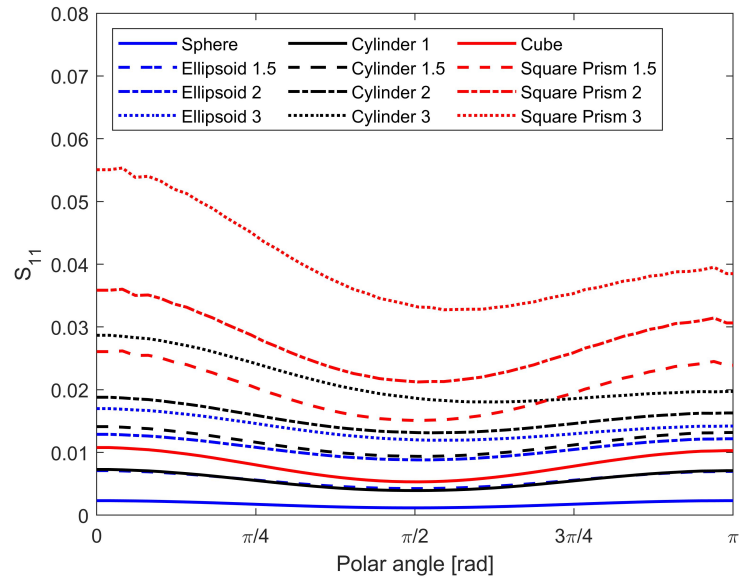
In contrast to the regression analysis, the aspect ratio and the edge are the dominant factors for the change in aspect ratio and edge. The incident wavelength has already been eliminated as we are only to the resonance wavelengths. Although size is one of the two main factors in all spectral domain, it is the least important when considering resonance wavelengths.

## 4.2. Directional Distribution of Scattered Intensity

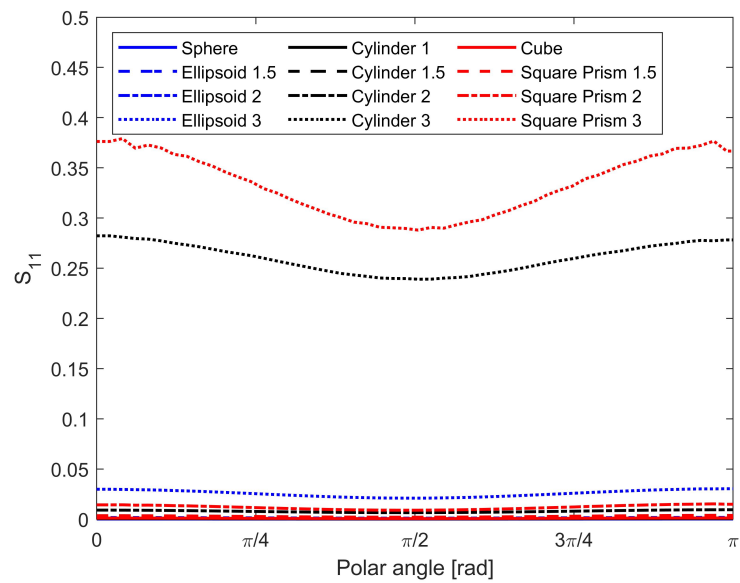
The scattering efficiencies were presented in the previous section to see at which wavelengths the nanoparticles exhibit the resonance peaks. Now the scattering dispersion is investigated using the polar angles of NPs. The  $S_{11}$  value is the scaled version of the scattering phase function presented earlier. The  $S_{11}$  values are examined at wavelengths of  $\lambda = 520, 540, 550, 570, 580, 610, 650, 720$  nm, which are the wavelengths of the individual resonance peaks. The results for the lowest wavelength  $\lambda = 520$  nm and the highest wavelength  $\lambda = 720$  nm are shown in Figure 4.18 for all nanoparticles with the same size with  $D = 50$  nm, blue lines for sphere and ellipsoids, black lines for cylinders and red lines for cube and square prisms. The graphs for  $S_{11}$  at the other wavelengths can be found in Appendix B. The absolute value of  $S_{11}$  is related to the scattering cross section and efficiency, which is also given in Equation (2.12). Thus, when the particle is close to its resonance wavelength, the  $S_{11}$  values become higher. As can be seen in Figure 4.18, the aspect ratio and existence of edges increase the  $S_{11}$  values.

Since the  $S_{11}$  values depend on the scatter and the larger the objects are, the more they scatter. To understand the  $S_{11}$  distribution over the polar angle, a normalization of these values should be done. Therefore, Figure 4.19 is created by dividing each  $S_{11}$  value by its maximum value for the lowest wavelength  $\lambda = 520$  nm and the highest wavelength  $\lambda = 720$  nm as in Figure 4.18. The particles whose resonance wavelength is close to the incident wavelength at  $\lambda = 520$  nm demonstrate a symmetrical trend across the polar angle. The particles whose resonance wavelength is not close have an asymmetric  $S_{11}$  across polar angle. As can be seen in Figure 4.19a, as the aspect ratio increases, the asymmetry of the  $S_{11}$  values increases at lower wavelengths. Existence of edges also increases the asymmetry. At the higher wavelengths which in Figure 4.19b, a higher aspect ratio does not cause asymmetry because the particles with higher aspect ratio have closer resonance wavelength. To distinguish the presence of corners,  $S_{11}$  values of the cylinder and the square prism can be compared. The ratio of maximum

and minimum value is higher for the prisms than for the cylinders at higher wavelengths for the particles that have the same aspect ratio.

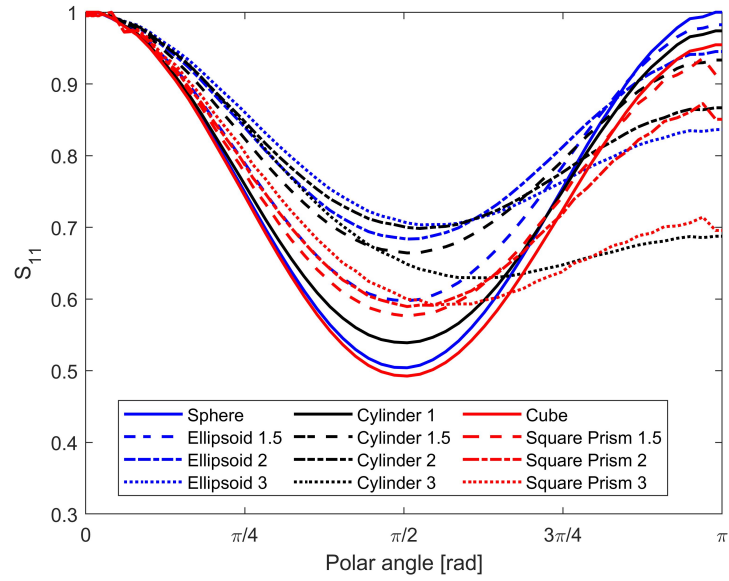


(a)

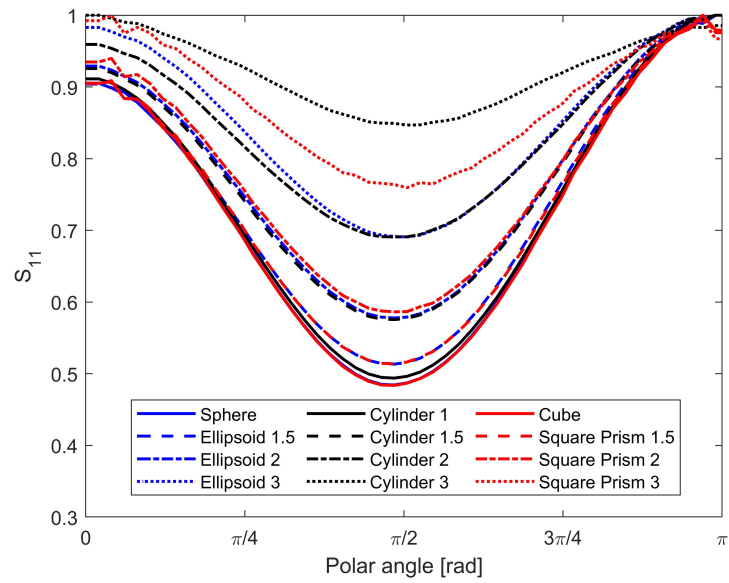


(b)

Figure 4.18.  $S_{11}$  values over polar angle for a) lowest  $\lambda = 520$  nm and b) highest  $\lambda = 720$  nm incident wavelength.



(a)



(b)

Figure 4.19. Normalized  $S_{11}$  values over polar angle for a) lowest  $\lambda = 520$  nm and b) highest  $\lambda = 720$  nm incident wavelength.

The nominal and normalized  $S_{11}$  values that are depicted in Figures 4.18 and 4.19 give a picture for evaluating the dispersion of the scattered electric field of the particles but it is not convenient to analyse it with multiple incident wavelengths due to the number of particles. Hence, the asymmetry in the  $S_{11}$  values can be defined by the asymmetry factor (AF) to analyse the scattering behaviour of the at different wavelengths. The asymmetry factor can be defined as the ratio of the total forward scattering to total backward scattering, whose formula is as follows:

$$AF = \frac{\int_{\theta=0}^{\pi/2} S_{11} d\theta}{\int_{\theta=\pi/2}^{\pi} S_{11} d\theta}. \quad (4.1)$$

This asymmetry factor is calculated for each NP and the results are demonstrated in Figure 4.20 to compare the edge effects. For each particle, the asymmetry factor decreases with increasing incident wavelength, which means that backward scattering increases with increasing wavelength. The presence of edges causes a higher asymmetry factor for each wavelength, which means that the edges increase the forward scattering. The values of AR are close for cylinders and prisms, so it is not useful to predict the presence of edges based only on AF. To understand the difference, the change of the  $S_{11}$  value over the polar angle should be investigated, which is already discussed and shown in Figure 4.18 and Figure 4.19.

The AF values are also compared with another combination to show the effects of aspect ratio, shown in Figure 4.21. A higher aspect ratio results in a higher AF, means the higher forward scattering. At lower wavelengths, the difference between AF is greater for the particles with higher and lower aspect ratios.

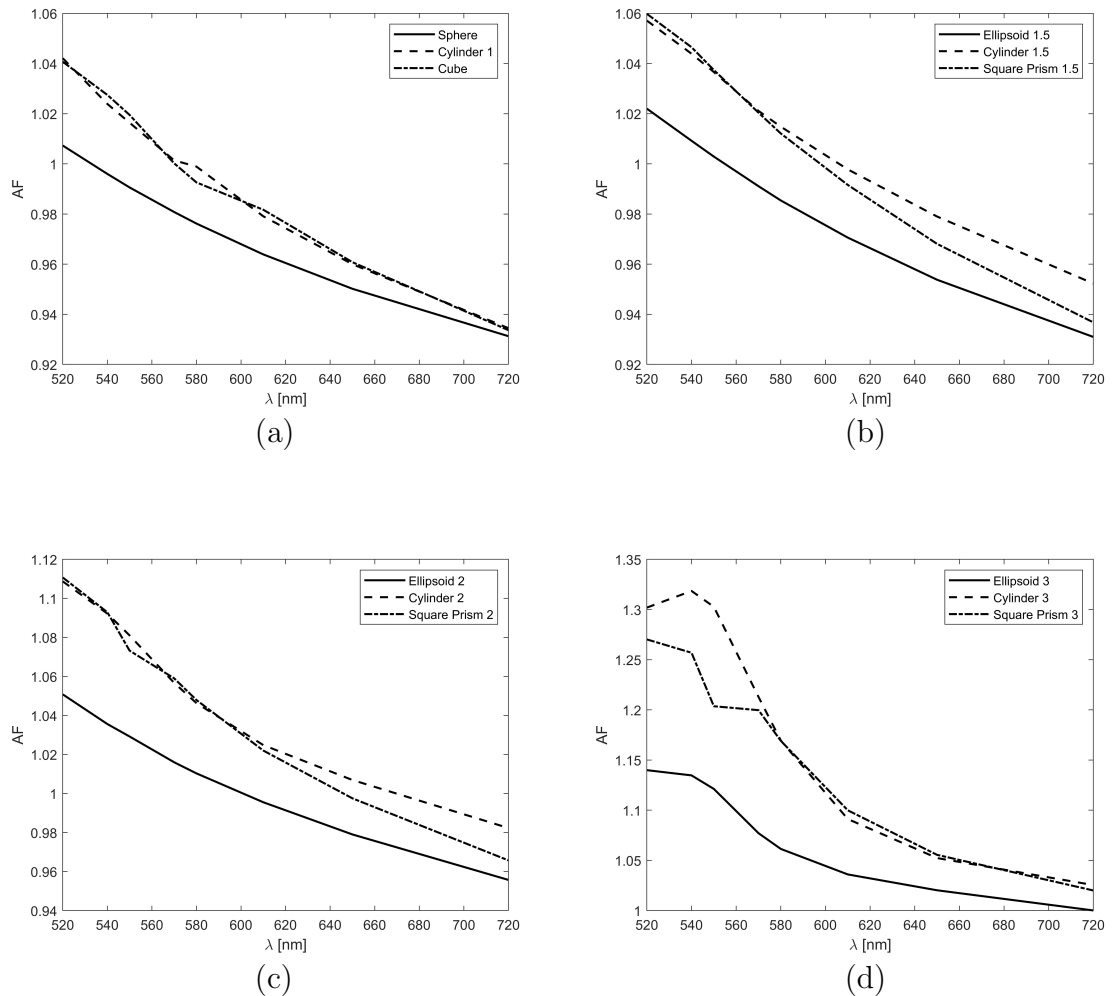


Figure 4.20. Asymmetry factors at different wavelengths for particles a) AR1 b) AR1.5 c) AR2 d) AR3.

A sensitivity analysis is carried out, as is done in calculations of scattering efficiency to understand the importance of parameters for the asymmetry factor. As already explained for the sensitivity analysis of the scattering efficiencies, it cannot be done in the same way because the increase in the parameters is not constant, but it can still give insight into the importance of the parameters. A pareto chart is given in Figure 4.22, which shows the impact of the parameters on AF. The aspect ratio is the most important parameter affecting the asymmetry of the  $S_{11}$  values, followed by the edge. The incident wavelength is the least important factor affecting the asymmetry of the scattered light.

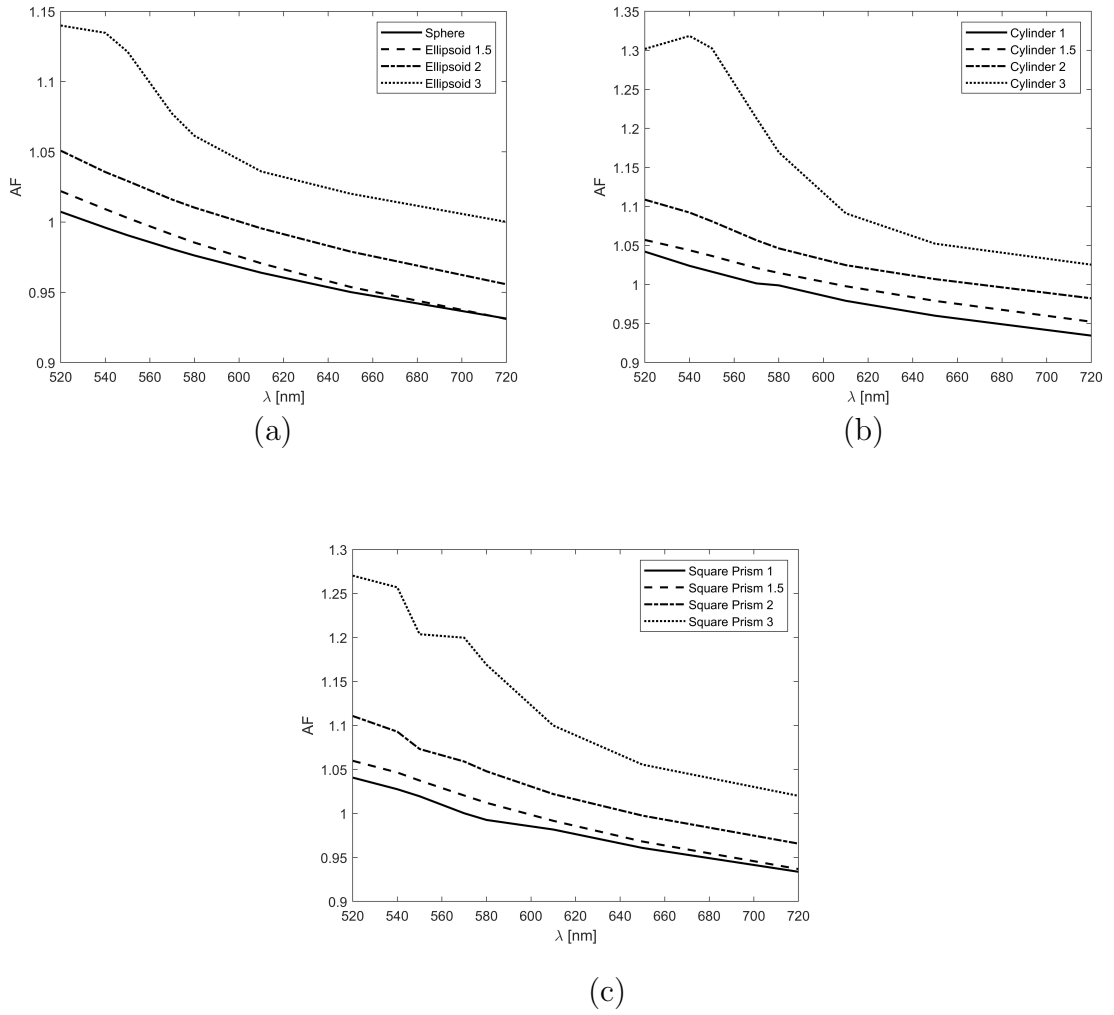


Figure 4.21. Asymmetry factors at different wavelengths for particles a) Spheroid b) Cylinder c) Prism.

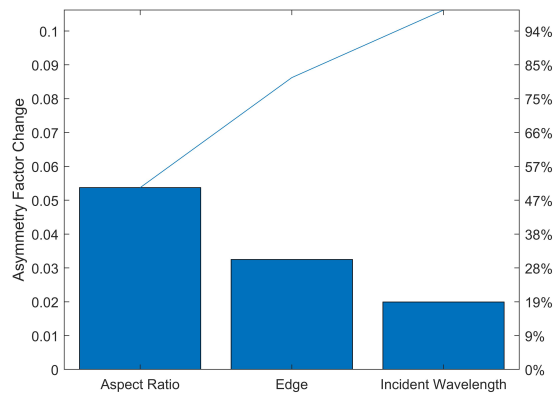


Figure 4.22. Pareto chart for asymmetry factors.

## 5. CONCLUSIONS

With the development of nanotechnology and its general application, the detection and characterization of these nanoparticles becomes a significant and difficult problem. These nanoparticles can be characterized from various aspects, and optical methods are common and efficient way to detect and characterize them. Although absorption effects are mainly studied to understand the nature of nanoparticles, scattering effects can also provide insights. Most studies are limited to specific materials and shapes and usually focus on resonance peaks. The aim of this work is to investigate the scattering effects of AuNPs by considering not only the resonance peaks, but also the scattering of different nanoparticles in terms of size and shape. To achieve this goal, FEM is created in the COMSOL program and the results are compared with the analytical Mie solution and other work. To achieve convergence of the results, mesh refinement and orientation averaging is performed for the particles. After the model is verified, the simulations are performed for the particles described in the problem statement.

All results are collected and compared to identify behavioural differences between NP. All of the findings on these differences that would help identify NPs can be summarized as:

- The effects of size on scattering efficiency change depending on the aspect ratio of the nanoparticles. At lower wavelengths, the increase in size only leads to an increase in scattering efficiency. It has no significant effect on the resonance wavelength. However, an increase in size does not increase the scattering efficiency but causes a red shift in the resonance wavelength.
- Increasing the aspect ratio causes both an increase in the efficiency values and a red shift in the resonance wavelength. It is also the main factor for the change in scattering efficiency and resonance efficiency according to the sensitivity analysis.
- Edge effects also change depending on the aspect ratio of the nanoparticles. Both

edge effects and corner effects are distinguishable when the aspect ratio is 1. However, corner effects cannot be observed because the efficiencies of the prism and cylinder follow the same trend across wavelengths, even though edge effects are still detectable. The presence of edges causes the increase in scattering efficiencies.

- The nominal values and asymmetry of  $S_{11}$  vary between nanoparticles. The nominal values are high for the particles that scatter more, are larger, have a higher aspect ratio and have edges. The asymmetry of the particles is also higher for the same changes.
- The distance to the resonance wavelength is the main reason for the asymmetry of  $S_{11}$  over the polar angle. The particles that are close to the resonance wavelength show symmetrical  $S_{11}$  dispersion. The aspect ratio is the main reason for the change in the asymmetry factor.
- An increase in size, aspect ratio and the presence of edges increases the forward scattering but an increase in incident wavelength has the opposite effect and causes an increase in backward scattering.

These analyses for scattering efficiencies and  $S_{11}$  values have shown that scattering parameters can be used to detect and characterise nanoparticles. Size and shape (elongation and edges) affect the scattering of a particle and these differences can be measured to understand the nanoparticle. The meshing and orientation averaging calculations also provide a guide to the convergence of results for each NP. This study also opens the door for some future work on nanoparticle characterization using scattering parameters:

- The measure points of the parameters can be selected according to principles of design of experiment. This would allow to provide more data and statistical interpretation of the data would be easier and useful.
- The calculation times are higher in COMSOL even though it allows to work with different particles easily. More rapid program such as DDA or DDSCAT can be used to obtain more data so that some machine learning algorithms can be

utilized to interpret the effects of parameters.

- Since the FEM allows to create and work on different particles, similar analysis can be conducted with the particles that have different sizes, shapes, materials and surrounding mediums. Different parametric analyses can be carried out by changing one or more of these parameters.
- This study is concerned with particles in suspension, but particles on surfaces are another challenging topic to investigated and it can also be analysed using FEM. Scattering from both the surface and the particles can interfere with each other and may provide a way to detect or characterise the nanoparticles.

## REFERENCES

1. Singh, V., S. S. Yadav, V. Chauhan, S. Shukla and K. K. Vishnolia, *Applications of Nanoparticles in Various Fields*, IGI Global, USA, 2021.
2. Sahu, M. K., “Semiconductor Nanoparticles Theory and Applications”, *International Journal of Applied Engineering Research*, Vol. 14, No. 2, pp. 491–494, 2019.
3. Salata, O. V., “Applications of Nanoparticles in Biology and Medicine”, *Journal of Nanobiotechnology*, Vol. 2, No. 1, pp. 1–6, 2004.
4. Pathakoti, K., M. Manubolu and H.-M. Hwang, “Nanostructures: Current Uses and Future Applications in Food Science”, *Journal of Food and Drug Analysis*, Vol. 25, No. 2, pp. 245–253, 2017.
5. Ramrakhiani, M., “Nanostructures and Their Applications”, *Recent Research in Science and Technology*, Vol. 4, No. 8, 2012.
6. Modena, M. M., B. Rühle, T. P. Burg and S. Wuttke, “Nanoparticle Characterization: What to Measure?”, *Advanced Materials*, Vol. 31, No. 32, p. 1901556, 2019.
7. Titus, D., E. J. J. Samuel and S. M. Roopan, *Green Synthesis, Characterization and Applications of Nanoparticles*, Elsevier, Amsterdam, 2019.
8. Bellare, J., H. Davis, W. Miller and L. Scriven, “Polarized Optical Microscopy of Anisotropic Media: Imaging Theory and Simulation”, *Journal of Colloid and Interface Science*, Vol. 136, No. 2, pp. 305–326, 1990.
9. Zhou, W., R. Apkarian, Z. L. Wang and D. Joy, “Fundamentals of Scanning Electron Microscopy (SEM)”, *Scanning Microscopy for Nanotechnology: Techniques and Applications*, pp. 1–40, 2007.

10. Hayat, M., *Basic Techniques for Transmission Electron Microscopy*, Elsevier, Amsterdam, 2012.
11. Rugar, D. and P. Hansma, “Atomic Force Microscopy”, *Physics Today*, Vol. 43, No. 10, pp. 23–30, 1990.
12. Russ, J. C., *Fundamentals of Energy Dispersive X-ray Analysis: Butterworths Monographs in Materials*, Butterworth-Heinemann, Oxford, 2013.
13. Ojeda, C. B. and F. S. Rojas, “Recent Developments in Derivative Ultraviolet/Visible Absorption Spectrophotometry”, *Analytica Chimica Acta*, Vol. 518, No. 1-2, pp. 1–24, 2004.
14. Lyon, L. A., C. D. Keating, A. P. Fox, B. E. Baker, L. He, S. R. Nicewarner, S. P. Mulvaney and M. J. Natan, “Raman Spectroscopy”, *Analytical Chemistry*, Vol. 70, No. 12, pp. 341–362, 1998.
15. Smith, B. C., *Fundamentals of Fourier Transform Infrared Spectroscopy*, CRC press, Boca Raton, 2011.
16. Iwashita, N., *Materials Science and Engineering of Carbon*, Elsevier, Oxford, 2016.
17. Chastain, J. and R. C. King Jr, *Handbook of X-ray Photoelectron Spectroscopy*, Perkin-Elmer Corporation, Massachusetts, 1992.
18. Goldberg, W. I., “Dynamic Light Scattering”, *American Journal of Physics*, Vol. 67, No. 12, pp. 1152–1160, 1999.
19. Nizamov, S., S. D. Sazdovska and V. M. Mirsky, “A Review of Optical Methods for Ultrasensitive Detection and Characterization of Nanoparticles in Liquid Media with a Focus on the Wide Field Surface Plasmon Microscopy”, *Analytica Chimica Acta*, Vol. 1204, p. 339633, 2022.

20. Anker, J. N., W. P. Hall, O. Lyandres, N. C. Shah, J. Zhao and R. P. Van Duyne, “Biosensing with Plasmonic Nanosensors”, *Nature Materials*, Vol. 7, No. 6, pp. 442–453, 2008.
21. Sevenler, D. and M. Selim Ünlü, “Numerical Techniques for High-throughput Reflectance Interference Biosensing”, *Journal of Modern Optics*, Vol. 63, No. 11, pp. 1115–1120, 2016.
22. Galy, T., D. Huang and L. Pilon, “Revisiting Independent versus Dependent Scattering Regimes in Suspensions or Aggregates of Spherical Particles”, *Journal of Quantitative Spectroscopy and Radiative Transfer*, Vol. 246, p. 106924, 2020.
23. Dombrovsky, L., “Radiative Properties of Single Particles and Fibers: the Hypothesis of Independent Scattering and the Mie Theory”, <https://www.thermopedia.com/content/136/>, accessed on November 12, 2022.
24. Amirjani, A., F. Firouzi and D. F. Haghshenas, “Predicting the Size of Silver Nanoparticles from Their Optical Properties”, *Plasmonics*, Vol. 15, pp. 1077–1082, 2020.
25. Pathak, N. K. and R. Sharma, “Study of Broadband Tunable Properties of Surface Plasmon Resonances of Noble Metal Nanoparticles using Mie Scattering Theory: Plasmonic Perovskite Interaction”, *Plasmonics*, Vol. 11, pp. 713–719, 2016.
26. Gharibshahi, E. and M. Alamaniotis, “Simulation and Modeling of Optical Properties of U, Th, Pb, and Co Nanoparticles of Interest to Nuclear Security Using Finite Element Analysis”, *Nanomaterials*, Vol. 12, No. 10, p. 1710, 2022.
27. Yang, S.-e., P. Liu, Y.-j. Zhang, Q.-N. Guo and Y.-s. Chen, “Effects of Silver Nanoparticles Size and Shape on Light Scattering”, *Optik*, Vol. 127, No. 14, pp. 5722–5728, 2016.

28. Jain, P. K., K. S. Lee, I. H. El-Sayed and M. A. El-Sayed, “Calculated Absorption and Scattering Properties of Gold Nanoparticles of Different Size, Shape, and Composition: Applications in Biological Imaging and Biomedicine”, *The Journal of Physical Chemistry B*, Vol. 110, No. 14, pp. 7238–7248, 2006.
29. Kluczyk, K. and W. Jacak, “Damping-induced Size Effect in Surface Plasmon Resonance in Metallic Nano-particles: Comparison of RPA Microscopic Model with Numerical Finite Element Simulation (COMSOL) and Mie Approach”, *Journal of Quantitative Spectroscopy and Radiative Transfer*, Vol. 168, pp. 78–88, 2016.
30. Mock, J., M. Barbic, D. Smith, D. Schultz and S. Schultz, “Shape Effects in Plasmon Resonance of Individual Colloidal Silver Nanoparticles”, *The Journal of Chemical Physics*, Vol. 116, No. 15, pp. 6755–6759, 2002.
31. Shen, H., G. Lu, T. Zhang, J. Liu, Y. Gu, P. Perriat, M. Martini, O. Tillement and Q. Gong, “Shape Effect on a Single-Nanoparticle-Based Plasmonic Nanosensor”, *Nanotechnology*, Vol. 24, No. 28, p. 285502, 2013.
32. Ringe, E., M. R. Langille, K. Sohn, J. Zhang, J. Huang, C. A. Mirkin, R. P. Van Duyne and L. D. Marks, “Plasmon Length: A Universal Parameter to Describe Size Effects in Gold Nanoparticles”, *The Journal of Physical Chemistry Letters*, Vol. 3, No. 11, pp. 1479–1483, 2012.
33. Lee, K.-S. and M. A. El-Sayed, “Dependence of the Enhanced Optical Scattering Efficiency Relative to that of Absorption for Gold Metal Nanorods on Aspect Ratio, Size, End-cap Shape, and Medium Refractive Index”, *The Journal of Physical Chemistry B*, Vol. 109, No. 43, pp. 20331–20338, 2005.
34. Zou, S. and G. C. Schatz, “Narrow Plasmonic/Photonic Extinction and Scattering Line Shapes for One and Two Dimensional Silver Nanoparticle Arrays”, *The Journal of Chemical Physics*, Vol. 121, No. 24, pp. 12606–12612, 2004.

35. Tamaru, H., H. Kuwata, H. T. Miyazaki and K. Miyano, “Resonant Light Scattering from Individual Ag Nanoparticles and Particle Pairs”, *Applied Physics Letters*, Vol. 80, No. 10, pp. 1826–1828, 2002.
36. Moghadam, F. R., “Optical Scattering Investigation of a Nonabsorbent Silicon Nanoparticles Array”, *Optik*, Vol. 201, p. 163477, 2020.
37. Thiele, E. S. and R. H. French, “Light-Scattering Properties of Representative, Morphological Rutile Titania Particles Studied Using a Finite-Element Method”, *Journal of the American Ceramic Society*, Vol. 81, No. 3, pp. 469–479, 1998.
38. Khoury, C. G., S. J. Norton and T. Vo-Dinh, “Plasmonics of 3-D Nanoshell Dimers Using Multipole Expansion and Finite Element Method”, *ACS Nano*, Vol. 3, No. 9, pp. 2776–2788, 2009.
39. Liu, L. and M. I. Mishchenko, “Effects of Aggregation on Scattering and Radiative Properties of Soot Aerosols”, *Journal of Geophysical Research: Atmospheres*, Vol. 110, No. D11, 2005.
40. Liu, C., R. L. Panetta and P. Yang, “The Influence of Water Coating on the Optical Scattering Properties of Fractal Soot Aggregates”, *Aerosol Science and Technology*, Vol. 46, No. 1, pp. 31–43, 2012.
41. Howell, J., R. Siegel, K. Daun and M. Menguc, *Thermal Radiation Heat Transfer*, CRC Press, Boca Raton, 2020.
42. Bohren, C. F. and D. R. Huffman, *Absorption and Scattering of Light by Small Particles*, John Wiley & Sons, New Jersey, 2008.
43. Luo, M. R., *Encyclopedia of Color Science and Technology*, Springer, New York, 2016.
44. Muinonen, K., “Light Scattering by Gaussian Random Particles: Rayleigh and

- Rayleigh-Gans Approximations”, *Journal of Quantitative Spectroscopy and Radiative Transfer*, Vol. 55, No. 5, pp. 603–613, 1996.
45. Draine, B. T. and P. J. Flatau, “Discrete-dipole Approximation for Scattering Calculations”, *Journal of the Optical Society of America A*, Vol. 11, No. 4, pp. 1491–1499, 1994.
  46. Loke, V. L., M. P. Mengüç and T. A. Nieminen, “Discrete-dipole Approximation with Surface Interaction: Computational Toolbox for MATLAB”, *Journal of Quantitative Spectroscopy and Radiative Transfer*, Vol. 112, No. 11, pp. 1711–1725, 2011.
  47. Wriedt, T., “Using the T-matrix Method for Light Scattering Computations by Non-axisymmetric Particles: Superellipsoids and Realistically Shaped Particles”, *Particle & Particle Systems Characterization*, Vol. 19, No. 4, pp. 256–268, 2002.
  48. Yee, K., “Numerical Solution of Initial Boundary Value Problems Involving Maxwell’s Equations in Isotropic Media”, *IEEE Transactions on Antennas and Propagation*, Vol. 14, No. 3, pp. 302–307, 1966.
  49. Sadiku, M. N., “A Simple Introduction to Finite Element Analysis of Electromagnetic Problems”, *IEEE Transactions on Education*, Vol. 32, No. 2, pp. 85–93, 1989.
  50. Rakić, A. D., A. B. Djurišić, J. M. Elazar and M. L. Majewski, “Optical Properties of Metallic Films for Vertical-Cavity Optoelectronic Devices”, *Applied Optics*, Vol. 37, No. 22, pp. 5271–5283, 1998.
  51. Etchegoin, P. G., E. Le Ru and M. Meyer, “An Analytic Model For the Optical Properties of Gold”, *The Journal of Chemical Physics*, Vol. 125, No. 16, p. 164705, 2006.
  52. Grand, J. and E. C. Le Ru, “Practical Implementation of Accurate Finite-

- Element Calculations for Electromagnetic Scattering by Nanoparticles”, *Plasmonics*, Vol. 15, No. 1, pp. 109–121, 2020.
53. Loke, V. L., G. Huda, E. Donev, V. Schmidt, J. Hastings, M. P. Mengüç and T. Wriedt, “Comparison between Discrete Dipole Approximation and Other Modelling Methods for the Plasmonic Response of Gold Nanospheres”, *Applied Physics B*, Vol. 115, pp. 237–246, 2014.
54. Laven, P., “MiePlot v4.6”, <http://www.philiplaven.com/mieplot.html>, accessed on October 19, 2022.
55. Penttilä, A. and K. Lumme, “Optimal Cubature on the Sphere and Other Orientation Averaging Schemes”, *Journal of Quantitative Spectroscopy and Radiative Transfer*, Vol. 112, No. 11, pp. 1741–1746, 2011.

## APPENDIX A: FINITE ELEMENT MODEL IN COMSOL

The finite element model is explained previously in general terms in Section 2.2. A detailed version of the finite element model that is created in COMSOL is given in this appendix to enable other readers to reproduce the same results and develop the model further. The formulation is given in COMSOL nomenclature for easier implementation. The tool-specific names are used throughout the text with initial capital letters to differentiate them from common terminology. The node tree of the COMSOL RF module can be seen in Figure A.1, which facilitates the understanding of the nodes in the model, which will be explained in the following sections.

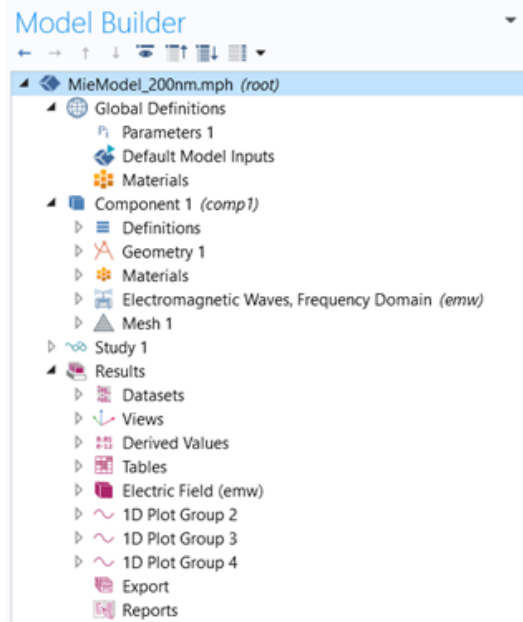


Figure A.1. Model node tree in COMSOL.

In COMSOL model, the global definitions are first established in the system. In Parameters node, the necessary parameters are defined that will be used throughout the model. An example of Parameters can be found in Table A.1 for the case when the nanoparticle is a sphere.

Table A.1. Parameters inputs in Global Definitions group.

Name	Expression	Value	Description
E0	1[V/m]	1 V/m	Electromagnetic field
r	25	25	Radius of the sphere
r_domain	10*r	250	Radius of domain
t_pml	3*r	75	Thickness of PML
lambda	300	300	Wavelength
lambda_min	300	300	Minimum wavelength
lambda_max	800	800	Maximum wavelength
lambda_step	10	10	Wavelength step size
geom_cs	$\pi*r^2$	3.1416E-14 m <sup>2</sup>	Geometric cross section
S_in	$E0^2/(2 * Z0_{const})$	0.0013272 W/m <sup>2</sup>	Incident wave intensity

The definition of the intensity of the incident waves (S\_in) is already set in Equation (2.5).  $Z0_{const}$  is the free space impedance built into COMSOL and its definition is also given in Equation (2.6).

After defining the parameters in the Global Definition group, the second step is to create the geometry in the Components group. The built-in geometry node in COMSOL allows the user to create an appropriate geometry for the problem. The geometry of the system is explained previously and depicted in Figure 2.2.

The next step in the model is the Definitions node in the Components group to define the necessary variables and functions for the models and the desired optical properties. In the Variables subgroup, these optical properties are defined, such as the Poynting vector, scattering, absorption, and extinction cross sections, and the corresponding efficiencies, which are listed in Table 2.2 but explained with COMSOL nomenclature in Table A.2 In the Artificial Domains subgroup, the Perfect Matched Layer option is added and the domains are selected to be created in the geometry.

Table A.2. Entries in Variables Subgroup.

Name	Expression	Unit	Description
nrelPoav	$nx*emw.relPoavx+$ $ny*emw.relPoavy+$ $nz*emw.relPoavz$	$W/m^2$	Poynting vector
C_sc	$intop\_surf(nrelPoav)/S\_in$	$m^2$	Scattering cross section
Q_sc	$C\_sc/geom\_cs$		Scattering efficiency

In Table A.2;  $nx$ ,  $ny$  and  $nz$  are normal vectors;  $emw.relPoavx$ ,  $emw.relPoavy$ ,  $emw.relPoavz$  are components of the time-averaged Poynting vector of the scattered field.  $intop\_surf$  and  $intop\_vol$  are the surface and volume integrals of nanoparticle, respectively. The integrals can be defined under the Definitions group and nanoparticle can be selected for the volume integral and surfaces of nanoparticle can be selected for the surface integral.

The material selection and physics of the system is already explained in Section 2. Nanoparticle domain is assigned as gold and the rest of it defined as air including PML. The background electric field is given in Table 2.1. The meshing of the system and mesh refinement are also explained in Sections 2 and 3.

When the  $emw$  Physics node is selected, the Wave Equation is automatically defined beneath the node. Electric displacement field and magnetic field must be chosen as the material's relative permittivity and relative permeability, respectively. Internal PML surfaces should be assigned Scattering Boundary Condition. Far Field Domain is an additional function of this node that calculates far field scattering in the geometry.

The final step is to define the Study nodes. Frequencies are defined as,

$$\nu = c\_const/lambda \tag{A.1}$$

in the Frequency Domain, where `c_const` is the built-in term for speed of light in free space. Parametric Sweep is also selected for parametric analysis over a range of wavelengths. Parameter is selected and the table is populated in Table A.3.

Table A.3. Parametric Sweep for wavelength analysis.

Parameter Name	Parameter Value List	Parameter Unit
lambda	range(lambda_min,lambda_step,lambda_max)	nm

These terms are already defined in the Global Definitions section of the model. Since all necessary points have been defined, the study can be conducted and results obtained.

When the Study is complete, the results node displays the calculated results. Some results are displayed automatically due to the use of `emw Physics` and the far field range, such as the resulting electric field and the 2D and 3D distributions of the far field. In addition, additional results that are the focus of this study can be derived from previously obtained data. In the Derived Values subgroup, the absorption and scattering efficiencies are calculated using global evaluations. By selecting Study 1/Solution 1, one can obtain them for a single wavelength, or for multiple wavelengths by selecting Study 1/Parametric Solutions 1.

The parametric surface for  $S_{11}$  calculation is also given with parametric surface in Table 2.3 and Figure 2.4. Once the surface is defined, the  $S_{11}$  values can be exported to a text file using the Export Data option. Equation (2.11) is written for the expression part using COMSOL nomenclature:

$$S_{sc} = \text{sqrt}(\text{emw.relPoavx}^2 + \text{emw.relPoavy}^2 + \text{emw.relPoavz}^2) \quad (\text{A.2})$$

$$S_{11} = S_{sc} * (2 * \text{pi} * 7 * r / \text{lambda})^2 / S_{in} \quad (\text{A.3})$$

The radius is defined as  $7r$  since the parametric distance is defined at the inner surface of PML.  $\lambda$  is the specific wavelength that  $S_{11}$  values are calculated, which are peak resonance wavelengths for this analysis.

## APPENDIX B: ADDITIONAL PLOTS

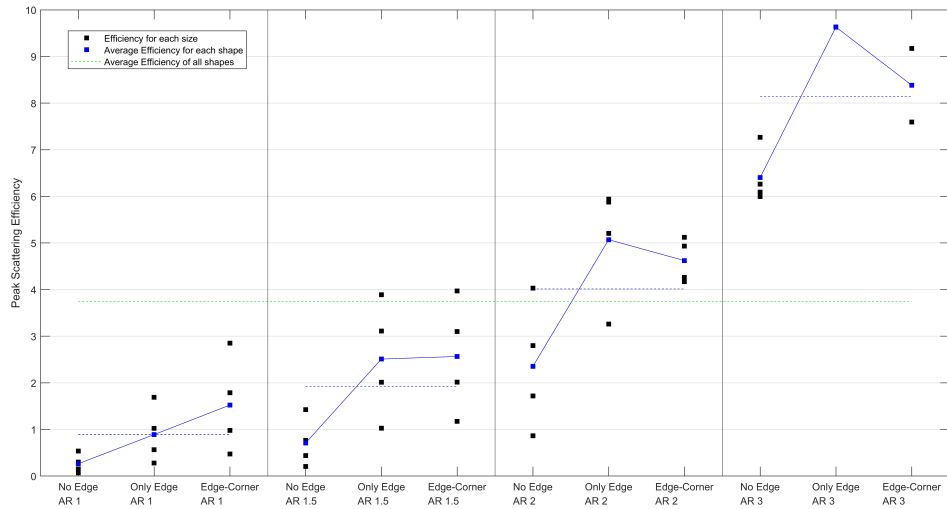


Figure B.1. Variability chart for the peak scattering efficiency.

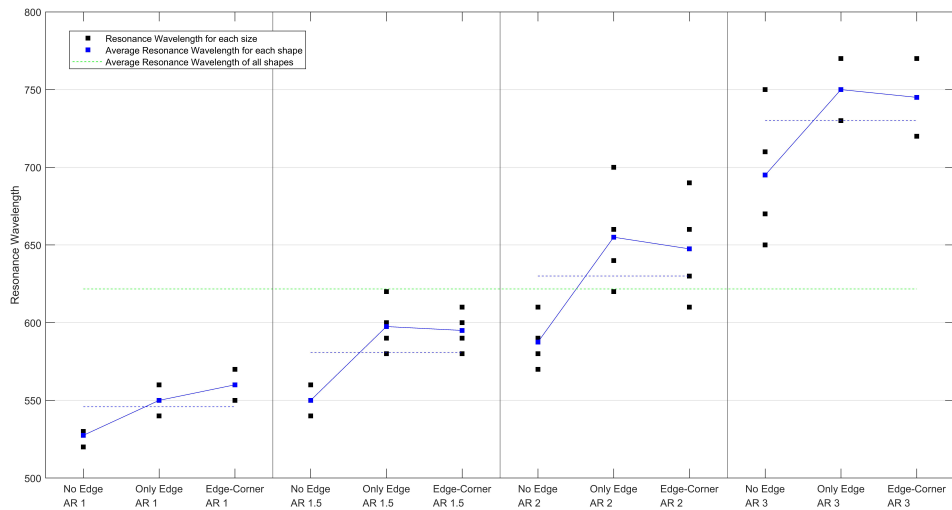


Figure B.2. Variability chart for the resonance wavelength.

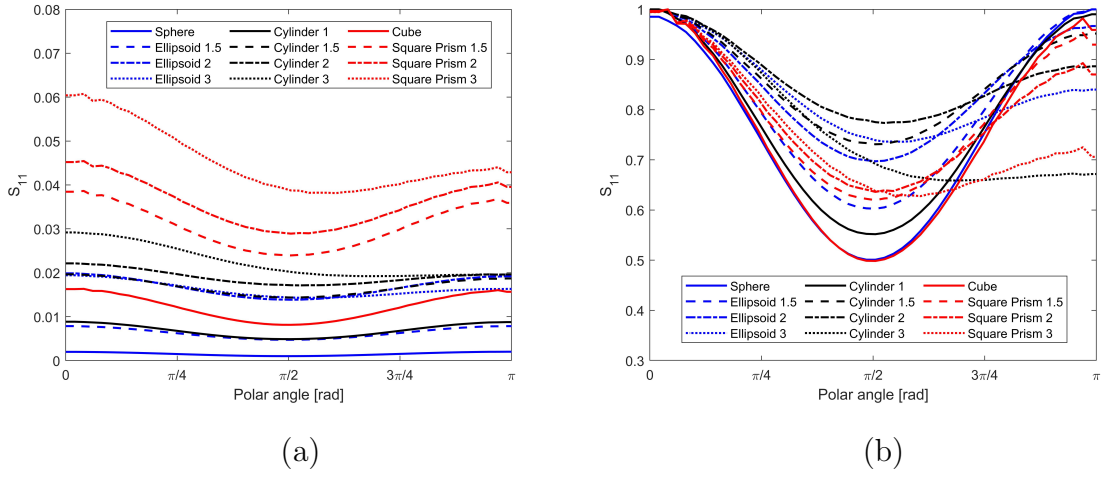


Figure B.3. a) Nominal b) Normalized  $S_{11}$  values over polar angle for  $\lambda = 540$  nm.

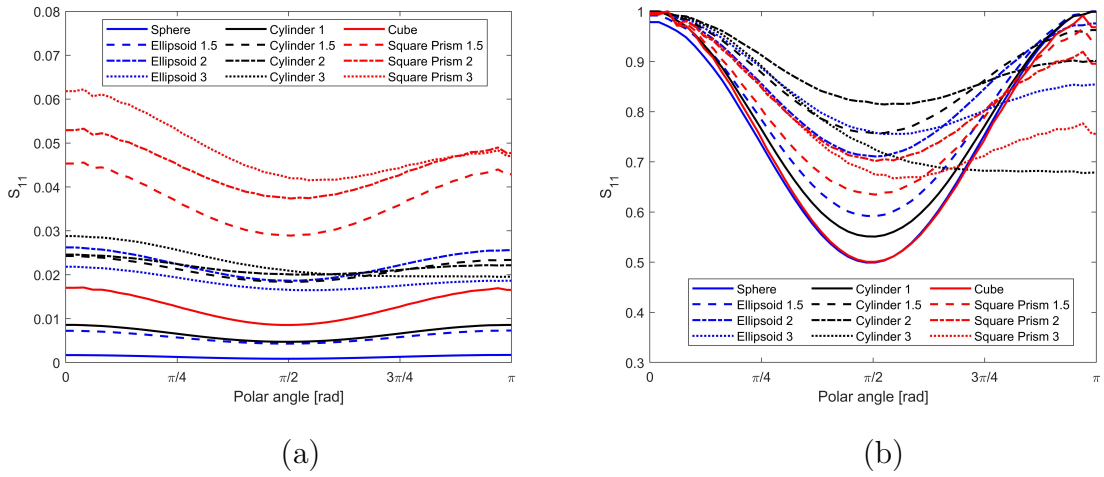


Figure B.4. a) Nominal b) Normalized  $S_{11}$  values over polar angle for  $\lambda = 550$  nm.

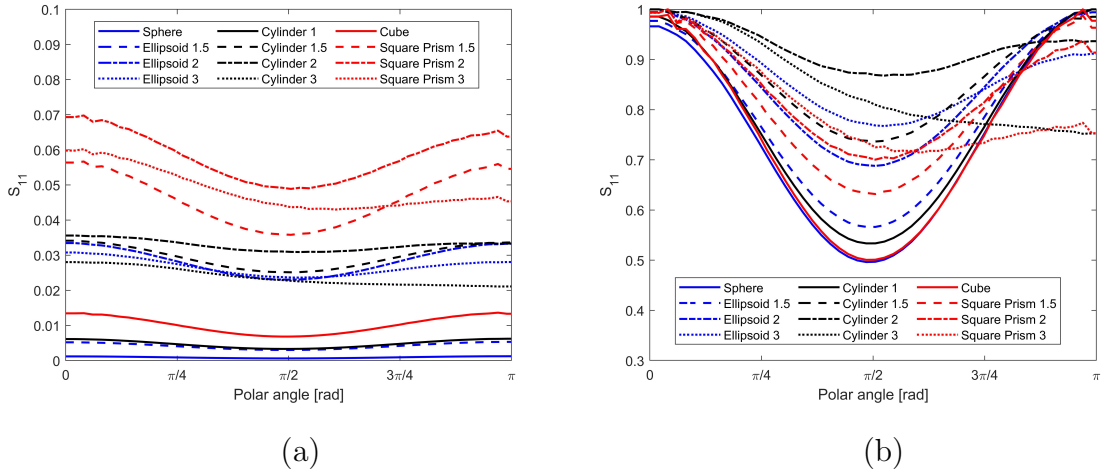


Figure B.5. a) Nominal b) Normalized  $S_{11}$  values over polar angle for  $\lambda = 570$  nm.

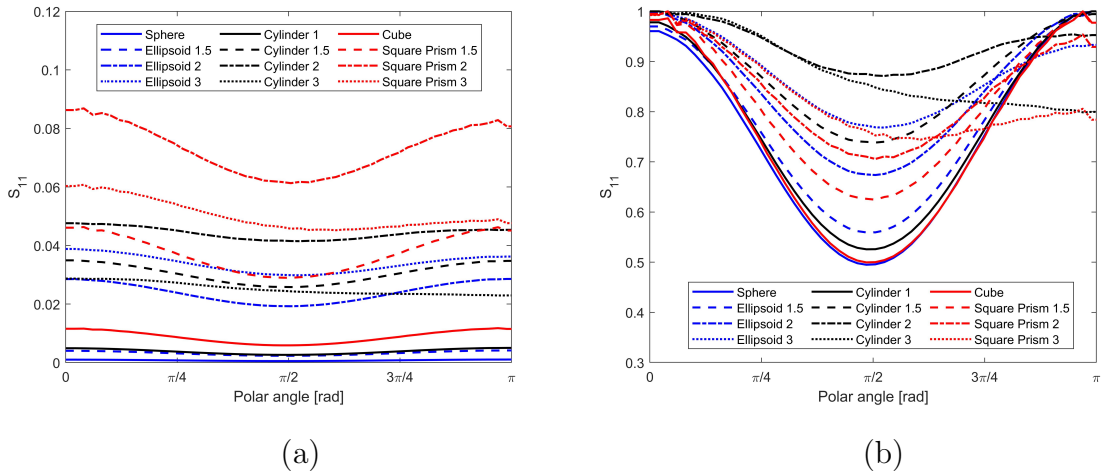
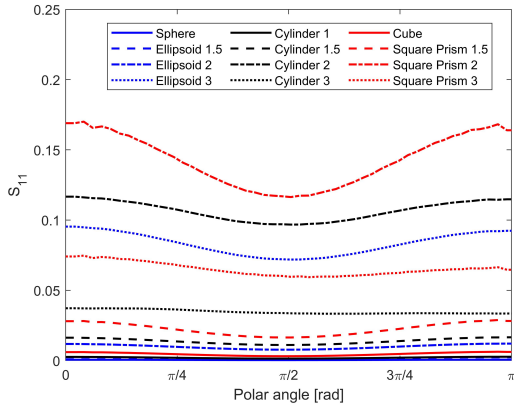
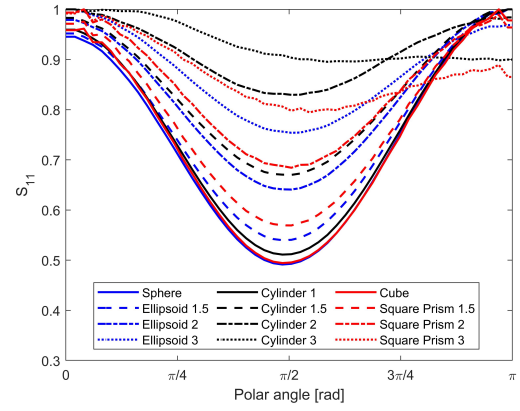


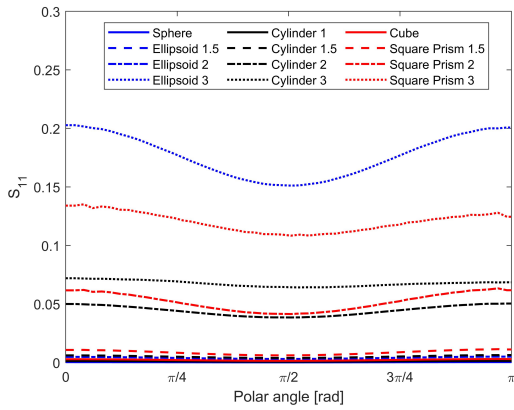
Figure B.6. a) Nominal b) Normalized  $S_{11}$  values over polar angle for  $\lambda = 580$  nm.



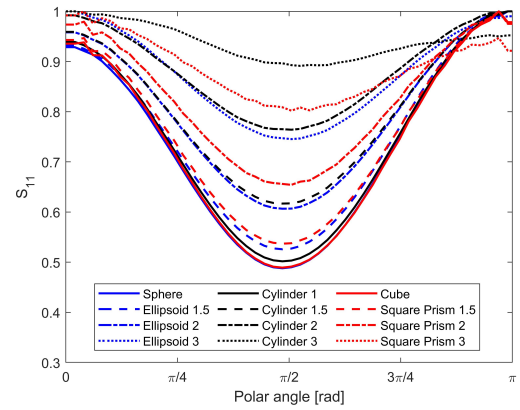
(a)



(b)

Figure B.7. a) Nominal b) Normalized  $S_{11}$  values over polar angle for  $\lambda = 610$  nm.

(a)



(b)

Figure B.8. a) Nominal b) Normalized  $S_{11}$  values over polar angle for  $\lambda = 650$  nm.